Fiber to Waveguide Couplers for Silicon Photonics

by

Trisha M. Montalbo

Submitted to the Department of Materials Science and Engineering
in partial fulfillment of the requirements for the degree of

Master of Science in Materials Science and Engineering

at the

MASSACHUSETTS INSTITUTE OF TECHNOLOGY

September 2004

Author .....
Department of Materials Science and Engineering
August 13, 2004

Certified by .....
Lionel C. Kimerling
Thomas Lord Professor of Materials Science and Engineering
Thesis Supervisor

Accepted by .....
Carl V. Thompson
Chair, Departmental Committee on Graduate Students

Fiber to Waveguide Couplers for Silicon Photonics

by

Trisha M. Montalbo

Submitted to the Department of Materials Science and Engineering
on August 13, 2004, in partial fulfillment of the
requirements for the degree of
Master of Science in Materials Science and Engineering

Abstract

As silicon photonics enters mainstream technology, we find ourselves in need of methods to seamlessly transfer light between the optical fibers of global scale telecommunications networks and the on-chip waveguides used for signal routing and processing in local computing networks. Connecting these components directly results in high loss from their unequal sizes. Therefore, we employ a coupler, which acts as an intermediary device to reduce loss through mode and index matching, and provide alignment tolerance.

This thesis presents a potential fiber-to-waveguide coupler design for use in integrating such networks. A quadratic index stack focuses incident light from a fiber in one plane, while a planar lens and linear taper do likewise in the perpendicular plane. Once the mode is sufficiently compressed, the light then enters and propagates through the waveguide. We performed simulations using the beam propagation method and finite difference time domain, among other modeling techniques, to optimize coupling efficiency and gain an understanding of how varying certain parameters affects coupler performance. The simulation results were then incorporated into a mask layout for fabrication and measurement.

Thesis Supervisor: Lionel C. Kimerling
Title: Thomas Lord Professor of Materials Science and Engineering

Acknowledgments

Many thanks to those who have helped me survive the past two years. It wasn't easy, but I couldn't have done it without their support. First and foremost is Kim, for always making time for me. His insight and support, both in research and in how to keep me motivated, were there when I needed them most. Anu and Kazumi were wonderful for discussions, technical and otherwise. Anu is so easy to talk to and has been incredible for hashing out ideas and how things work. And without Jurgen's practical knowledge on our labs, I don't think I could have accomplished anything, much less cleaned up HF spills. Finally, I'm grateful to Mindy for letting me go shopping at VWR as often as I wanted.

A big thank you goes to the students in EMAT for their friendship early on and making me feel welcome even when I was in my own little world of silicon electrochemistry. However, there are some I have to mention in particular, starting with Victor for teaching me all about the coupler. I'll not easily forget the weekend hours we spent with LayoutPlus, putting the mask together although without Ching-Yin, the two of us would have been working at it for many more weekends. Jeff—not an EMAT member, but this past year he's come close—has been incredibly patient with all my questions about simulations. To all those with porous silicon—Luca, Yasha, David, and Tongyan—thanks for letting me abandon that project so I would have time to finish this thesis. All in all, I couldn't have asked for a better group.

Finally, I want to thank my parents for their support from afar and my friends here in Cambridge, in particular Justin who provided hugs, motivation, and sympathy work, and Jeremy for distraction breaks with bridge and MarioKart.

Contents

List of Figures

List of Tables

Chapter 1

Introduction

To date, engineering has done a remarkable job of maintaining the exponential growth of the solid-state circuit industry, both in increasing the number of transistors per circuit and in decreasing the cost per transistor [4]. This rate of growth conforms to Moore's original observation, noted almost 40 years ago, that the number of integrated circuit components per chip, based on the minimum manufacturing cost per component, will approximately double every one to two years [5]. Each time we believe we are approaching the barrier to improving performance, the industry manages to creatively sidestep the obstacle. For example, switching over from use of aluminum and silicon dioxide as interconnect and gate materials, respectively, to copper and low κ-materials has allowed us to lower RC delays and continue with the current method of reducing transistor gate length to improve performance [1]. However, it's clear we are nearing the limits of microelectronics technology—this time for real. As gate length decreases, interconnect length and complexity increase so that, by some future technology generation, interconnects are expected to dominate delay time (Figure 1-1).

Silicon microphotonics offers a potential solution to sidestepping this so-called "red brick wall" and continuing the increase of data density. In photonics, photons rather than electrons transmit information; this significantly increases the maximum transmission capacity. Additionally, the approach eliminates cross-talk and has negligible heat dissipation, thus doing away with problems that plague current

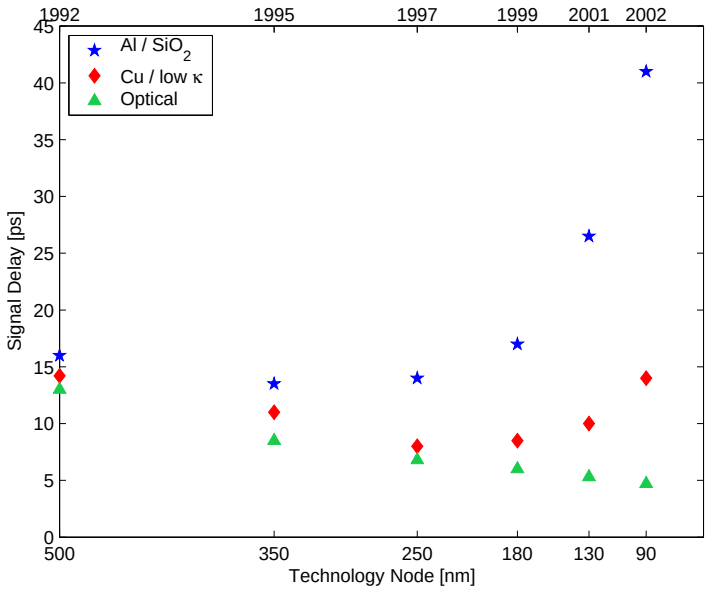

Figure 1-1: Signal delay for different transistor generations [1, 2, 3].

microelectronics technology [3]. Furthermore, a silicon-based platform permits use of well-characterized materials and existing processing techniques, as well as allowing for monolithic integration with control and drive electronics [6]. Already, the telecommunications industry relies on fiber optic cables to accommodate its need for large bandwidth information transfer on a global scale. Smaller scale microphotonics for computing technology is still under development so this market continues to rely on microelectronics although at present, nearly all necessary components have been demonstrated in research labs [1]. However, in order to attain the all optical network of the future, work remains for us in the interconnection and integration of those components within the constraints of silicon microphotonics [7].

1.1 Defining of Problem

Optical fibers that transmit data over long distances will form the backbone of our future all optical network and connect computer boards and chips containing waveguides, detectors, filters, and other devices for signal processing and routing. From an interconnection standpoint, we need to pass data not only between on-chip devices, but also from fiber-to-chip and vice versa. Doing this efficiently requires that we

consider optical alignment and mode mismatch between devices, and general losses from interconnection [7]. For fiber-to-chip coupling, this is not an easy task owing to the differing sizes of the two cores. Typical single mode fibers have a core diameter of 8 μm; high index contrast waveguides ($\Delta n \geq 0.5$) have cores ≤ 1 μm. Consequently, transferring light directly between these two components results in high power loss.

The standard solution to this problem is to insert an intermediary component between the fiber and the waveguide, known as an optical coupler, which receives light from the fiber and efficiently transmits it to the waveguide. Different variations of this component exist [8]. Our particular design is composed of a graded index stack of silicon oxynitride layers and a lateral, linear taper with a planar lens. The graded index stack vertically focuses light into the waveguide while the taper and planar lens do likewise in the horizontal plane. Thus the fiber mode is reshaped into the waveguide mode by the end of the coupler.

1.2 Thesis Outline

This thesis focuses on optimizing the coupler design described above through various simulation methods. These methods, along with the theoretical background of couplers and requirements we need to meet to attain a high coupling efficiency, are described in Chapters 2 and 3. We detail our approach to device optimization in Chapter 4 and briefly discuss some of the constraints under which we are working. These simulation results are then used in the mask layout so we can confirm our understanding of how controlled changes to the optimized design affect coupler performance. Chapter 5 covers the mask layout as well as the fabrication process and additional variations that arise in fabrication but that we did not account for in the initial simulations of Chapter 4. Our design is contrasted with other coupler designs in Chapter 6 and we discuss if our coupler meets the requirements laid out in Chapter 2. Finally, the conclusions in Chapter 7 wrap up the thesis by discussing future work in coupler fabrication and measurement, and the role silicon photonics may eventually play in our future.

Chapter 2

Theory

We start off this thesis with the theory of waveguides and couplers before discussing the simulation techniques used to study these devices. Although simulations may be sufficient to intuitively understand how a device functions, they cannot always explain why it behaves as it does. Some knowledge of theory is necessary to do this, as well as to develop the initial design in the first place. This same knowledge is also useful in interpreting simulation results because we will be able to determine if the results fundamentally make sense or if there is a potential problem in our design or modeling approach.

2.1 Waveguides

Waveguides are optical components that direct the flow of light. They consist of a dielectric core and a lower refractive index cladding; light is confined to the core by total internal reflection. Typically waveguides are thought of as on-chip devices fabricated from pure silicon, silicon nitride, or other such materials, but optical fibers also fall under this general category because they rely on the same principles to perform similar functions.

When light is coupled to a waveguide, it can excite a particular electromagnetic field distribution that propagates unchanged through the structure. This field distribution is called a mode. Depending on cross-sectional geometry, core-cladding index

contrast, and the wavelength of the propagating field, a waveguide can support anywhere from one to ten or more modes. In the latter case, the waveguide is said to be *multimoded* and will typically have some combination of its modes excited upon the coupling of light to its core. The resulting field will change as it propagates due to phase differences between superposed modes and to *modal dispersion*, or the difference in group velocities of the modes. Ideally, we want to limit the waveguide to the first or *fundamental* mode; this simplifies our simulations and removes modal dispersion from the picture so our field is unchanging in space and time.

Since modes are simply electromagnetic field distributions propagating through media, they carry energy, determined by $\mathbf{E} \times \mathbf{H}$ integrated over a plane perpendicular to the propagation axis, where $\mathbf{E}$ and $\mathbf{H}$ are the electric and magnetic field strengths respectively. Higher order modes are more energetic. By limiting the integration to the core area, we can calculate P_{core}, the power in the core; likewise, we can also find the power in the cladding, P_{clad} by restricting the integration to the cladding region. $P_{core} + P_{clad}$ should yield the total power (or energy) of the mode. The power distribution of the mode can be used to calculate its *effective index*, n_{eff}, approximated by

$$n_{eff} = \frac{P_{core} n_{core} + P_{clad} n_{clad}}{P_{total}} \tag{2.1}$$

The effective index arises because energy travels in both the waveguide core and adjacent cladding. Cross-section boundary conditions dictate that $\mathbf{E}$ and $\mathbf{H}$ in the cladding decay exponentially as we move away from the core, perpendicular to the propagation axis.

2.1.1 Coupling Waveguides

For waveguides to be useful, we have to connect them to devices such as detectors and filters, to each other, or to the off-chip world. If the waveguides are physically different and therefore support different fundamental modes, this can present problems, particularly when butt-coupling the waveguides. For instance, the input fiber we use for our simulations has a 6 μm core and a low index contrast to limit it to

a single mode; in comparison, the on-chip waveguide we want to connect it to has a high index contrast and a 0.9 μm core. Assuming the two are perfectly joined end-to-end, we find that the loss is around 6.8 dB [9]. Thus, we need to place a fiber-to-waveguide coupler between the two to efficiently transfer light from one to the other. The requirements for such a coupler are reviewed in Section 2.2 and the remainder of this thesis focuses on the design of one of these devices.

2.1.2 Index Grading

Waveguides with graded index cores are useful for dealing with modal dispersion in multimode waveguides. Elimination of dispersion is accomplished with a quadratic index profile (Figure 2-1) waveguide to control group velocity and phase differences between modes. The index profile is typically described by the equation

$$n(r) = n_o \left(1 - \alpha r^2\right) \tag{2.2}$$

Lower order modes, which have higher group velocities and are concentrated near the waveguide center, are slowed down by the higher index material. On the other hand, higher order modes, which are more spread out with a larger fraction of power in the lower index material, are able to move faster. In the end, all modes have the same group velocity and dispersion is eliminated. Also, the energy difference between consecutive modes is constant for this particular profile, frequency increases by 2π for each increase in mode number. (This can be proved analytically in the 2D case, but the derivation will not be presented here [10, 11].) Therefore, when multiple modes propagate through the waveguide, they simultaneously move in and out of phase. This leads to the self-imaging phenomenon in which light focuses in the highest index region of the core before diverging to recreate the initial field distribution (composed of all excited modes). The process is then repeated periodically along the length of the waveguide as light focuses and diverges at regularly-spaced intervals. Our coupler uses a graded index stack that relies on this self-imaging effect to vertically focus light into the waveguide.

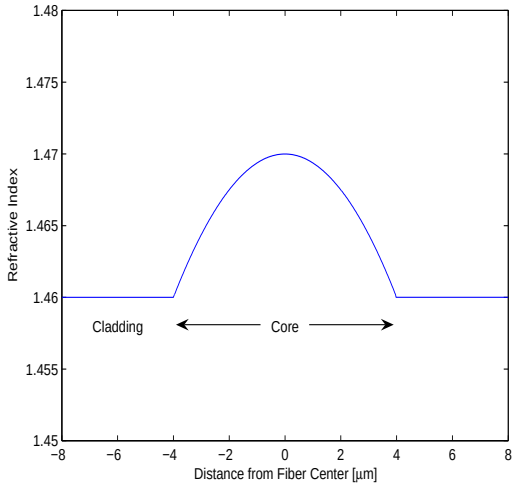

Figure 2-1: Sample parabolic profile of a graded index fiber.

2.2 Couplers

Optical couplers are devices used to interconnect photonic networks by connecting the components of one network to those of another. In the context of this thesis, couplers connect single mode optical fibers to on-chip single mode waveguides. Despite the fact that both these components only support one mode, their differing geometry causes a large mismatch between the two, which the coupler has to resolve. To do this, the coupler will have to address three primary issues:

- Mode matching and transformation
- Index difference
- Optical alignment

High coupling efficiency—the transferring light between disparate waveguides—is achieved if the coupler performs in all three areas.

2.2.1 Mode Matching and Transformation

As stated in Section 2.1.1, butt-coupling of a fiber directly to a waveguide will result in large losses from power coupled into to the cladding or to radiation modes (poorly

confined modes that eventually leak into the cladding). Thus, the ideal coupler should be able to match the mode of the fiber and losslessly transform it to an allowed propagation mode of the waveguide, while simultaneously collecting and transmitting as much of that light as possible. Mode matching avoids the excitation of radiation modes and light collection prevents losses to the cladding. Implementing this in a coupler is done in a variety of ways, either by adiabatic reshaping of the mode or with lenses or coupled resonators, among other approaches (see Section 6.1). Our coupler employs a graded index stack to change the mode vertically, and a taper and lens for horizontal reshaping.

2.2.2 Index Difference

In addition to matching and reshaping modes, a coupler also has to match effective indices with both components it connects. Failure to do this causes Fresnel reflections, which occur because the wave has to satisfy boundary conditions at the interface. For light at normal incidence, the ratios of reflected (R) and transmitted (T) power to incident power are given by

$$R = \left(\frac{n_2 - n_1}{n_2 + n_1}\right)^2 \tag{2.3}$$

$$T = \frac{4n_2n_1}{(n_2 + n_1)^2} \tag{2.4}$$

Reflections result in power loss and potential interference with the incident wave. For instance, if a fiber fundamental mode with an effective index of $n_{eff}^{(f)} \approx 1.47$ encounters a coupler input facet with $n_{eff}^{(c)} \approx 1.67$, 0.5% of the power is reflected, which amounts to a 0.02 dB loss.

2.2.3 Optical Alignment

All devices—not just couplers—have to be aligned with the path of the data signal in order to read or manipulate it. Given component dimensions, even a one micron offset can significantly impact transmission efficiency. Ultimately, alignment depends on

fabrication and packaging equipment accuracy: in simulation, we can easily suppose everything is perfectly aligned, but accomplishing this is too difficult in fabrication. Simulation, though, can be used to assess the affect of misalignment on performance.

2.3 Summary

Some knowledge of theory is essential when developing the initial concept and design of a device, and later on when running simulations to better understand the device's behavior. For instance, to create a waveguide coupler, one has to be aware of requirements like mode and index matching, as well as ways to translate those requirements into a physical design. Our coupler design requires additional knowledge of graded index waveguides and how quadratic grading in particular affects the flow of light. Afterwards, simulations can be used to impart an intuitive feel for how the coupler functions and how changing design parameters affect its performance. This can also be a check on the theoretical concepts behind the coupler: do the simulations match theory or were some of the initial assumptions fallacious? Finally, the fabrication of the device can be used to confirm both simulations and theory, and serve as the ultimate proof the coupler works.

Chapter 3

Simulation Methods

Simulations of the interaction of light with matter are an inexpensive and rapid method to gain an intuitive understanding of how various structures affect the transmission of light. With simulations, evaluating performance is far more rapid because fabrication time is no longer a factor. More importantly, they provide a starting point for fabrication by allowing us to dissect a device and its behavior so that the first trip to the cleanroom is not a shot in the dark. Furthermore, we have greater control over the important design parameters within a regulated environment.

However, simulations also have their limits: in an idealized environment, it is difficult, if not impossible, to account for everything that will affect the performance of an actual device. Therefore, despite their apparent usefulness, simulations provide only a partial insight into device's performance. Prototyping and testing are the best method for proving that the design indeed works. Secondly, most, if not all, simulations methods have drawbacks, whether in approximations assumed or in time limits owing to computational intensity. As a result, they can only provide us with an accurate picture of what will happen in limited ideal cases and are unable to take into account every potential parameter variation that may arise in experiment. But in combination with experiments, simulations are a powerful tool in device design. Depending on the complexity of the simulated device, we can work on the initial design and subsequent refinements iteratively, using simulations and device fabrication.

In this chapter, we review the simulation methods we use to evaluate device be-

havior. Both finite difference time domain (FDTD) and beam propagation method (BPM) allow us to study the propagation of light through our coupler and into a waveguide. From this, we can determine the optimal device dimensions—later used as the starting point for mask layout and fabrication. Ray matrices offer us another look at individual components of our structure, specifically the graded index stack and the lens. We use them either as a tool for quick verification of the more complex simulation methods, or as a simple technique to study the light paths through the graded index stack or lens. Finally, we use the effective index method to collapse a 3D structure into a 2D one so that we can reduce the number of dimensions we work with as well as simulation time.

3.1 Finite Difference Time Domain

3.1.1 Maxwell's Equations

Maxwell's equations are a set of four equations that describe the behavior of electromagnetic radiation. These equations were first presented by James Maxwell in 1864 and today are commonly written in differential form as

$$\nabla \times \mathbf{H} = \frac{\partial}{\partial t}\mathbf{D} + \mathbf{J} \tag{3.1}$$

$$\nabla \times \mathbf{E} = -\frac{\partial}{\partial t}\mathbf{B} \tag{3.2}$$

$$\nabla \cdot \mathbf{D} = \rho \tag{3.3}$$

$$\nabla \cdot \mathbf{B} = 0 \tag{3.4}$$

$\mathbf{E}$ and $\mathbf{H}$ are the electric and magnetic field strengths respectively, $\mathbf{D}$ the electric displacement, $\mathbf{B}$ the magnetic flux density, and $\mathbf{J}$ and ρ the current and charge density [12]. Since we are working in photonics, we are only interested in source-free situations so $\rho = 0$ and $\mathbf{J} = 0$. The equations simplify further if our material system

is isotropic:

$$\mathbf{D} = \epsilon\mathbf{E} \tag{3.5}$$

$$\mathbf{B} = \mu\mathbf{H} \tag{3.6}$$

where ϵ, the material permittivity and μ, the permeability, are scalars. In the end, we are left with

$$\nabla \times \mathbf{E} = \frac{\partial}{\partial t}\mu\mathbf{H} \tag{3.7}$$

$$\nabla \times \mathbf{H} = \frac{\partial}{\partial t}\epsilon\mathbf{E} \tag{3.8}$$

$$\nabla \cdot \mathbf{E} = 0 \tag{3.9}$$

$$\nabla \cdot \mathbf{H} = 0 \tag{3.10}$$

which the finite difference time domain (FDTD) method solves, following the Yee algorithm, to determine the behavior of **E** and **H** in a region of space over time.

3.1.2 The Yee Algorithm

The Yee algorithm, the basis of FDTD, provides a means to numerically solve for electric and magnetic fields in time over some region of space using Equations (3.7) and (3.8). The replacement of derivatives by finite differences is the only approximation used by the algorithm: everything else is exact. Numeric calculations then take place on a mesh overlying the spatial domain. However, because the primary equations used to solve for **E** and **H** are coupled, the two fields cannot be calculated at the same coordinate points. To resolve this issue, **E** is calculated on the original lattice and **H** on a second lattice displaced from the original by half a unit step in each direction (Figure 3-1) so that each **E** point is surrounded by four points at which **H** is calculated and vice versa. The fields are then alternately computed in time across the entire mesh. **E** (**H**) at any given point depends on its value at that point at an earlier time, and on the values of **H** (**E**) at the surrounding points [13].

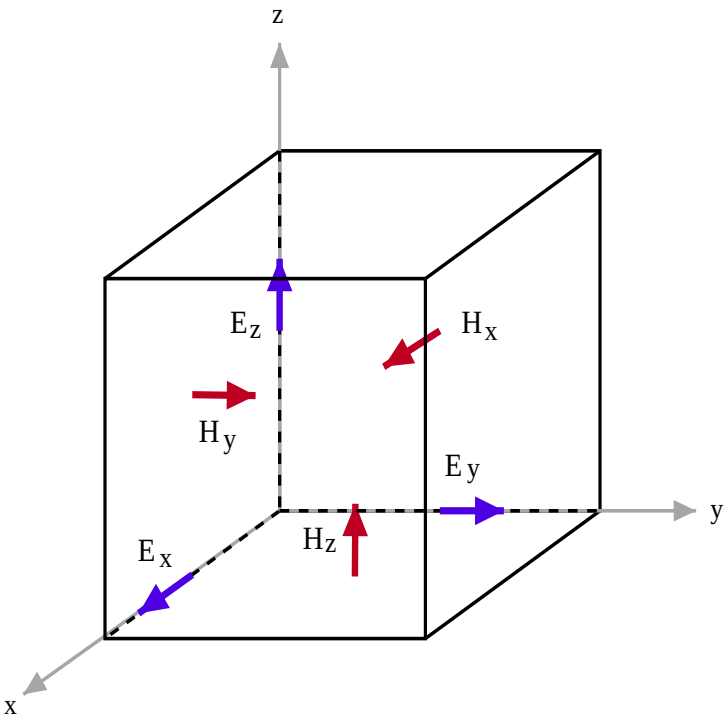

Figure 3-1: Electric and magnetic field components on a FDTD unit cell.

In order to accurately simulate electromagnetic fields with FDTD, the grid spacing has to be sufficiently small so that field strength does not appreciably change between adjacent grid points and that the finite difference approximation holds. This implies that for computational stability,

$$c\Delta t \leq \left(\frac{1}{(\Delta x)^2} + \frac{1}{(\Delta y)^2} + \frac{1}{(\Delta z)^2} \right) \tag{3.11}$$

has to be satisfied for spatial steps Δx, Δy, and Δz, and temporal step Δt. Also appropriate boundary conditions are needed or else extraneous reflections will be introduced at the edges of the computational domain and affect the simulation. Typically, perfectly matched layers are used. Developed by J.P. Berenger, this technique implements layers that absorb radiation without creating reflections at the simulation boundaries [14].

3.1.3 Coupler-Specific Considerations

The FDTD method is one of our two primary approaches—the other being BPM—to simulating our coupler structure. Because FDTD calculates **E** and **H** at numerous points in space over a period of time, it can produce accurate results, but is also computationally intensive, it's primary drawback. Consequently, we are able to handle only 2D simulations on our standard personal computers; evaluating 3D structures requires access to a supercomputer.

When working in 2D, we can separate the light into two polarizations: transverse electric (TE) and transverse magnetic (TM), as shown in Figure 3-2. If light propagates along the z-axis and the structure is defined in the xz-plane, then for TE polarization, **E** is perpendicular to the plane of incidence so $\mathbf{E} = \hat{y}E_y$ and $\mathbf{H} = \hat{x}H_x + \hat{z}H_z$ with all other components set to zero. The situation is similar for TM polarization except **E** and **H** trade places. Equations (3.7) and (3.8), when broken down into component vectors, become

$$\begin{aligned} \frac{\partial}{\partial z}E_y &= \mu\frac{\partial}{\partial t}H_x \\ \frac{\partial}{\partial x}E_y &= -\mu\frac{\partial}{\partial t}H_z \\ \frac{\partial}{\partial z}H_x - \frac{\partial}{\partial x}H_z &= \epsilon\frac{\partial}{\partial t}E_y \end{aligned} \tag{3.12}$$

for TE polarization and

$$\begin{aligned} -\frac{\partial}{\partial z}H_y &= \epsilon\frac{\partial}{\partial t}E_x \\ \frac{\partial}{\partial x}H_y &= \epsilon\frac{\partial}{\partial t}E_z \\ \frac{\partial}{\partial z}E_x - \frac{\partial}{\partial x}E_z &= -\mu\frac{\partial}{\partial t}H_y \end{aligned} \tag{3.13}$$

for TM polarization. If the grid spacings are equal so that $\Delta x = \Delta z = \Delta$, the stability criterion, Equation (3.11), simplifies to

$$c\Delta t \leq \frac{\Delta}{\sqrt{2}} \tag{3.14}$$

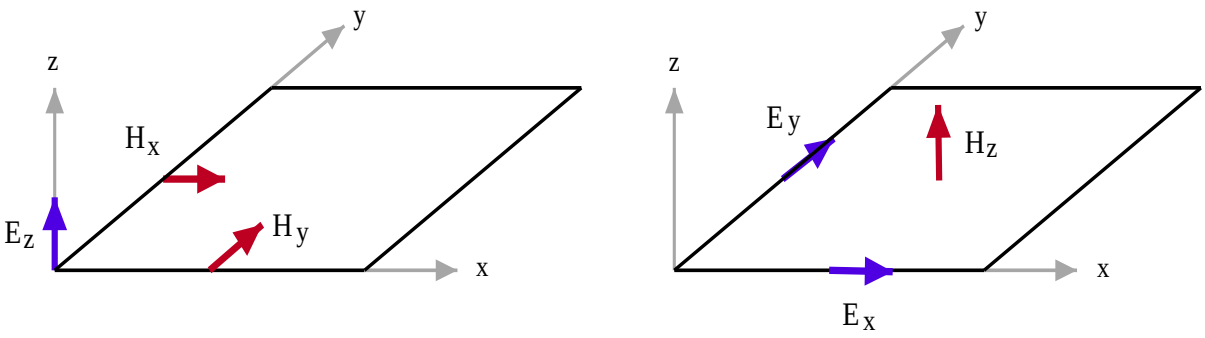

Figure 3-2: Two dimensional FDTD unit cells for TE and TM polarization.

To perform these simulations, we used FullWAVE^{TM}, a commercial FDTD simulation package produced by the RSoft Design Group. This software comes with a CAD (Computer Aided Design) layout program, which simplifies construction of devices for simulations. Simulations are run by defining a device through its dielectric structure and specifying parameters like wavelength, grid spacing, time step, and field profile of the radiation source. FullWAVE components, known as time monitors, calculate power, $\mathbf{E} \times \mathbf{H}$, as a function of time across a user-specified line segment.

All our simulations used a Gaussian source of an appropriate width to represent the input fiber mode. We used time monitors to evaluate power present in the waveguide relative to coupler input power so we could assess coupling efficiency and optimize this ratio through appropriate design modification. To meet the stability condition, we chose a grid size of $\Delta x = \Delta z = 0.05$ and $c\Delta t = 0.024$. Finally, we chose TE polarization for our simulations because this is the more lossy of the two polarizations and therefore gives us the upper limit on loss.

3.2 Beam Propagation Method

Our other simulation approach is the beam propagation method (BPM), which uses the Helmholtz wave equation to calculate how light propagates in media. Like FDTD, BPM calculates the electric field at points on a mesh overlying some spatial domain. However, instead of computing **E** and **H** at all possible points for each time step, it calculates the field on a plane perpendicular to the propagation axis then steps forward

in space to the next plane and repeats the calculation, continuing until the field along the length of the structure is known. In order to do this with the Helmholtz equation, BPM makes some assumptions about the propagating waves, as will be detailed in the following sections.

3.2.1 The Helmholtz Wave Equation

The Helmholtz equation is derived from the source-free Maxwell equations in isotropic media, Equations (3.7) to (3.10). By separating the fields into their components to obtain scalar partial differential equations, we can solve for E_x through elimination of H_x, H_y, and H_z:

$$\begin{aligned} 0 &= \left(\frac{\partial^2}{\partial x^2} + \frac{\partial^2}{\partial y^2} + \frac{\partial^2}{\partial z^2} - \mu\epsilon\frac{\partial^2}{\partial t^2}\right) E_x \\ &= \left(\nabla^2 - \mu\epsilon\frac{\partial^2}{\partial t^2}\right) E_x \end{aligned} \tag{3.15}$$

Doing likewise with E_y and E_z leaves us with three equations of the same form as Equation (3.15), which can be combined to give

$$0 = \left(\nabla^2 - \mu\epsilon\frac{\partial^2}{\partial t^2}\right) \mathbf{E} \tag{3.16}$$

The resulting wave equation signifies that $\mathbf{E}$ behaves as a wave with velocity $v = (\mu\epsilon)^{-1/2} = c/n$. The same equation can be derived for $\mathbf{H}$ and shows the quantity to be a wave with the same properties as $\mathbf{E}$.

3.2.2 BPM Approximations

BPM uses Equation (3.16) to calculate light propagation; however it first makes assumptions so that the equation easier to work with. First off, by taking $\mathbf{E}$ to be a scalar, the vector field can be replaced with $E(x, y, z, t) = \phi(x, y, z)e^{i\omega t}$ and the time derivative eliminated, leaving

$$0 = \left(\nabla^2 + k^2\right) \phi \tag{3.17}$$

where $k = \omega\sqrt{\mu\epsilon}$. The next approximation is to factor out rapid phase variations along the propagation axis. In doing this, we also assume that the wave predominantly travels along this axis, the z-axis, and so impose a paraxiality condition on simulations. Introducing a slowly varying field, u, to ϕ and removing phase variations gives us

$$\phi(x, y, z) = u(x, y, z)e^{i\bar{k}z}. \tag{3.18}$$

where $\bar{k}$ is a constant representing the average phase variation of ϕ. Substituting Equation (3.18) into Equation (3.17),

$$0 = \left(\frac{\partial^2}{\partial x^2} + \frac{\partial^2}{\partial y^2} + \frac{\partial^2}{\partial z^2}\right) u + \left(k^2 - \bar{k}^2\right) u + 2i\bar{k}\frac{\partial}{\partial z}u \tag{3.19}$$

If we next assume that u varies very slowly with z, we can eliminate $\frac{\partial^2 u}{\partial z^2}$ because the second order change will be much smaller than the first. Under this slowly varying envelope approximation, we finally arrive at

$$\frac{\partial}{\partial z}u = \frac{i}{2\bar{k}}\left[\frac{\partial^2}{\partial x^2}u + \frac{\partial^2}{\partial y^2}u + \left(k^2 - \bar{k}^2\right) u\right] \tag{3.20}$$

which is a first order initial value problem rather than a second order boundary value problem. To further reduce simulation calculations, only forward propagating solutions to Equation (3.20) are considered: backwards-traveling waves, including reflections, are assumed negligible. More advanced BPM approaches relax these approximations, but we will not cover them here.

As is typically the case, simplifying assumptions can be both beneficial and restrictive. Since the field is defined on a mesh, derivatives in Equation (3.20) become finite differences. With the revised Helmholtz equation, we can solve for the field in a structure by starting with an initial field distribution at one end and integrating Equation (3.20) on planes perpendicular to the propagation axis until the other end is reached. Factoring out rapid phase variations from the problem permits a coarser mesh along the propagation direction, thereby further decreasing calculation time. However, devices that depend on phase changes may not be suited for BPM

simulations because of the averaging of the phase variations. Also, the paraxial approximation excludes structures that allow waves to deviate at large angles from the axis, such as propagation from a waveguide into free space. Finally, the elimination of the second derivative in the slowly varying envelope approximation prevents Equation (3.20) from simultaneously dealing with forwards- and backwards-propagating solutions and only forward are considered to reduce computational intensity. The disregard for backwards-propagating waves means that BPM cannot accurately simulate structures with high index contrast along the propagation direction because it cannot account for the effect of reflected waves on the field distribution [15].

3.2.3 Coupler-Specific Considerations

Despite all the restrictions of BPM, it is still one of the more commonly used simulation methods. We rely on it for some aspects of our coupler and believe it to be reasonably accurate because its results are comparable to those of FDTD. Also, unlike FDTD, it can handle 3D simulations on a personal computer within reasonable amounts of time.

For our simulations, we used another RSoft software package, BeamPROP$^{\text{TM}}$, designed for BPM modeling. The package includes the same CAD layout program as FullWAVE, but we constructed different structures since all our FDTD simulations were run in 2D but BPM were done in 3D. As before, simulations are run by defining the dielectric structure of a device and specifying wavelength, grid spacing, field source profile, and so forth. However, instead of time monitors, BeamPROP evaluates power through mode overlap as a function of propagation distance using the equation

$$P = \int \int \psi_{ref}(x,y)\psi_{sim}(x,y)dA \tag{3.21}$$

where ψ_{ref} and ψ_{sim} are the normalized field distributions of a reference mode and the field within the simulated structure, respectively.

When running simulations, we relied on two reference modes (ψ_{ref}), the fiber fundamental mode and the waveguide fundamental mode, and plotted their overlap

with the field in our coupler. Optimizing coupling efficiency is equivalent to optimizing mode matching conditions—and therefore mode overlap—so that the maximum amount of power is transmitted through the coupler and into the waveguide. The same fiber fundamental mode, represented by a Gaussian, was used as the input source. Finally, we used a mesh with $\Delta x = \Delta y = 0.03$ and $\Delta z = 0.2$ to take advantage of the coarser grid spacing along z.

3.3 Ray Transfer Matrices

FDTD and BPM, even with restrictions, provide reasonably complete pictures of light propagation in media. They are able to simulate a number of devices from waveguides to ring resonators. However, they can also be time consuming—particularly 3D FDTD—and even with commercial simulation software, can still be confusing for the novice user.

Ray optics presents a simpler picture of light. Instead of oscillating waves, light is represented by rays that can reflect off surfaces or refract upon passing through an interface, but do not interfere with each other or create resonances. This picture is valid if the light wavelength is much larger than the structure dimensions.

A ray is defined as the normal to an optical wavefront and is represented by a vector containing its displacement from the propagation (z) axis and its angle with respect to that axis:

$$\begin{pmatrix} r(z) \\ \theta \end{pmatrix} \tag{3.22}$$

Typically θ is sufficiently small so that $\sin\theta \sim \theta$ and the paraxial approximation applies.

The interaction of rays with various optical elements can be described with transform matrices, that is, $[r_{out}] = [T][r_{in}]$. For instance, when a ray travels a distance of d through free space, its displacement with respect to the z-axis changes, but not its angle so $r_{out} = r_{in} + d\tan\theta_{in} \approx r_{in} + d\theta_{in}$ and $\theta_{out} = \theta_{in}$. The resulting matrix is

$$\begin{pmatrix} 1 & d \\ 0 & 1 \end{pmatrix} \tag{3.23}$$

Matrices for more complex optical elements can be derived, but we will not do so here (see [16] for details). Among the elements we are most interested in are spherical dielectric interfaces,

$$\begin{pmatrix} 1 & 0 \\ \frac{n_2-n_1}{n_2 R} & \frac{n_1}{n_2} \end{pmatrix} \tag{3.24}$$

where R, the radius of curvature, is positive if the interface is concave towards the incident ray and negative if convex. We will also employ the matrix for propagation in a medium with a quadratic index profile, defined by

$$n = n_o \left(1 - \frac{k_2}{2k} r^2\right) \tag{3.25}$$

The medium has the same effect as a lens on ray propagation:

$$\begin{pmatrix} \cos\left(\sqrt{\frac{k_2}{k}} z\right) & \sqrt{\frac{k}{k_2}} \sin\left(\sqrt{\frac{k_2}{k}} z\right) \\ -\sqrt{\frac{k_2}{k}} \sin\left(\sqrt{\frac{k_2}{k}} z\right) & \cos\left(\sqrt{\frac{k_2}{k}} z\right) \end{pmatrix} \tag{3.26}$$

Ray matrices fall far short of BPM and FDTD when it comes to understanding the interactions light with a device and evaluating performance. However, once derived, they are quick and easy to use to comprehend the direction of light flow. Also, they provide a means to concentrate on a single aspect or parameter of a device and investigate how a second parameter is affected by the first without having to worry about the larger picture.

3.4 Effective Index Method

Between BPM and FDTD, the latter is the better method to evaluate the effect of the lens on coupling efficiency. However, our FDTD software can only handle 2D simulations so it is unable to account for the effect of the graded index stack on mode

shape and effective index. To get around this, we used the effective index method (EIM) to collapse the 3D coupler into a 2D structure which FDTD can handle (see Section 4.1.3).

The effective index method translates the index a mode in a 3D structure sees to the core index of a slab waveguide in a 2D structure. The index depends on the mode number, wavelength, and device cross-section. We can only consider one mode at a time and that mode will vary with propagation distance because of the taper's changing cross-section. Although this approach doesn't provide us with an exact answer, it can still assist in creating an approximate picture of light interactions with a collapsed structure. The following derivation follows the one presented in [10].

EIM views the 2D slab waveguide as a finite potential well of width $2a$ centered at $x = 0$ and potential function

$$n = \begin{cases} n_{core} & |x| \leq a \\ n_{clad} & |x| > a \end{cases} \tag{3.27}$$

where n_{core} and n_{clad} are the core and cladding indices of the slab waveguide, respectively. Electromagnetic fields propagating in the waveguide are subject to the boundary conditions imposed by the potential function. Specifically, the longitudinal component of the field—in this case, the z component if the waveguide lies in the xz-plane—must be continuous across the core/cladding interface. (The transverse component also has to satisfy the same boundary condition for the slab waveguide, but we ignore it since it can be written in terms of the longitudinal component through Maxwell's equations.) Thus, the longitudinal component of a field propagating along the z-axis can be written as

$$H_z = h_z(x)e^{-i\beta z}e^{i\omega t} \tag{3.28}$$

where $h_z(x)$ is the field amplitude and the exponentials show that H_z oscillates in both space and time.

We chose H_z because we are assuming TE polarized light in the waveguide; therefore E_y is the transverse component and a function of H_z. Since H_z represents a

propagating magnetic field, it must also satisfy the Helmholtz equation. Substituting Equation (3.28) into Equation (3.16) gives us

$$0 = \frac{\partial^2}{\partial x^2} h_z(x) + \gamma^2 h_z(x) \tag{3.29}$$

$$\gamma^2 = n^2 k_o^2 - \beta^2 \tag{3.30}$$

k_o is the free space wave number and is equal to $2\pi/\lambda = \omega/c$. All that remains is to choose $h_z(x)$ such that the boundary conditions are satisfied. For a bound state (or mode),

$$h_z(x) = \begin{cases} A\cos(ux) + B\sin(ux) & |x| \leq a \\ Ce^{-w|x|} & |x| > a \end{cases} \tag{3.31}$$

so that it oscillates within the core, but decays in the cladding. If we ignore the sine term in Equation (3.31) and consider only cosine or even functions, we can solve for constants u and w by substituting Equation (3.31) into Equation (3.29):

$$u^2 = n_{core}^2 k_o^2 - \beta^2 \tag{3.32}$$

$$w^2 = \beta^2 - n_{clad}^2 k_o^2 \tag{3.33}$$

Together, u and w form a transcendental equation,

$$\tan(ua) = \frac{w}{u} \tag{3.34}$$

The number of solutions to this equation determines how many even TE modes exist in the waveguide. For the odd modes, we ignore the cosine term in Equation (3.31) instead and solve for u and w as before. Further math shows that a 2D waveguide will always support at least one even mode and zero or more odd modes.

The propagation constant, β, is determined by the effective index of the 3D mode:

$$\beta = n_{eff} k_o \tag{3.35}$$

In this manner, we can relate 3D structures to 2D ones and control how H_z propagates

along the z-axis and its spatial frequency (see Equation (3.28)). If we know β, n_{clad}, k_o, and a, we can calculate n_{core}, the core index of the collapsed 2D waveguide.

3.5 Summary

For our simulations, we primarily rely on FDTD and BPM to provide us with optimal dimensions for our coupler design as well as an intuitive picture of how light interacts with the structure. Although FDTD is limited to 2D simulations and BPM makes assumptions which may or may not be valid given our coupler, we believe a combination of these two techniques is sufficient for us to understand how varying design parameters affects coupling efficiency. In a few situations, ray matrices serve us better because they allow us to focus on how changing a single parameter affects a second parameter and eliminate the larger picture. They also have their restrictions but on the whole are a useful "quick and dirty" method to understanding the problem. Finally, EIM provides a means for us to collapse a 3D structure into two dimensions so that we can use FDTD. Even though it itself is an approximation and can only deal with a one mode even in multimoded structures, EIM opens the door to using both FDTD and BPM to study the same parameter so we can confirm our results. Of course, all simulations are performed in an idealized environment because it is nearly impossible to take every possible parameter into account without overly complicating the problem. Thus, the ultimate check will be whether experiment matches with the design simulations.

Chapter 4

Device Design

To optimize the coupler design and evaluate the effect of changing parameters on design performance, we relied on the combination of the simulation methods detailed in the preceding chapter. However, it is difficult for us to account for every design parameter in our simulations and optimize each one. Therefore, we limited ourselves to parameters essential to mask layout—specifically, coupler dimensions—and fixed the remaining parameters at appropriate values, chosen to satisfy fabrication or measurement preconditions. The parameters to be optimized include

- Coupler length
- Input facet width
- Output facet width
- Lens radius

They are illustrated in Figure 4-1. In Section 4.1, we outline our approach to optimizing each one. Fixed parameters include

Wavelength 1550 nm, one of the telecommunications wavelengths

Input fiber SMF28 (single mode fiber) with a 6 μm core diameter; from our calculations, this corresponds to a 6.2 μm mode field diameter.

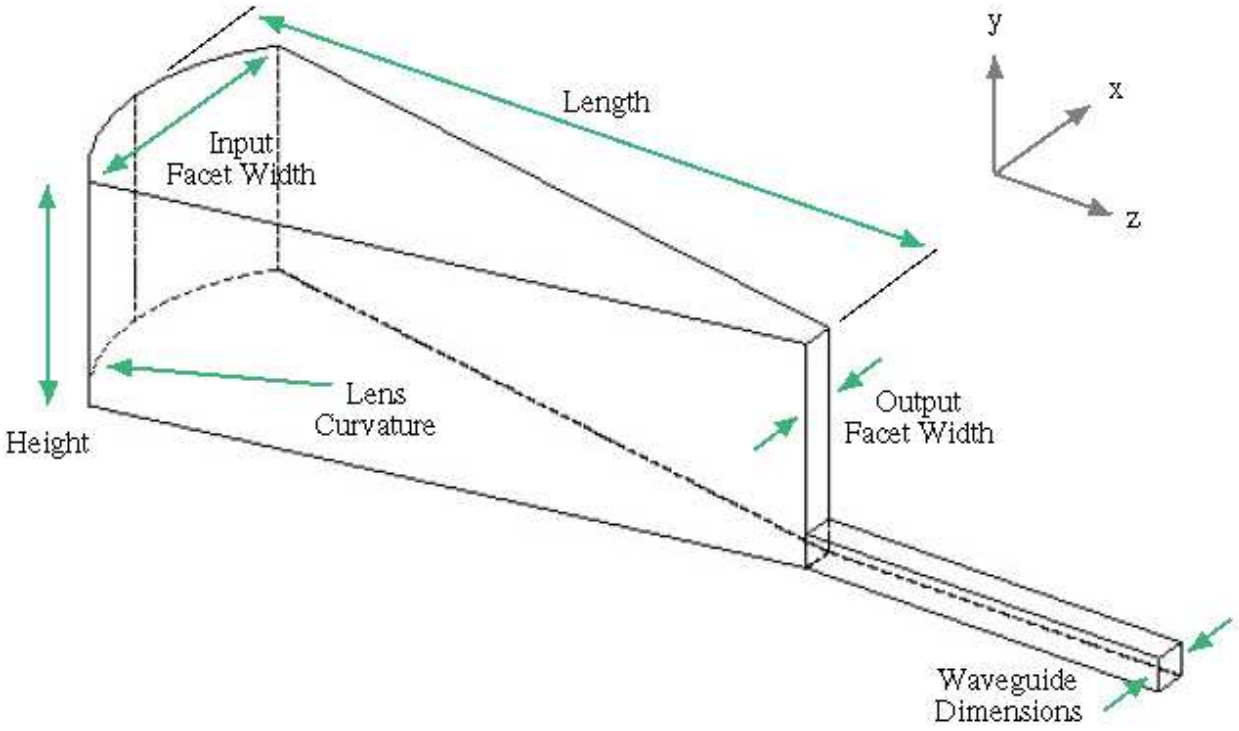

Figure 4-1: Coupler design parameters.

Stack grading profile defined as a seven-layer half-parabolic step profile starting at the waveguide index to the cladding index (Figure 4-2). We chose this profile to simplify the simulation layout and under the assumption that we will be able to grow all seven layers in the dielectric chemical vapor deposition (DCVD) chamber.

Stack height 6 μm, the height we have been working with in developing the fabrication process, particularly the stack etch step.

Stack taper linear, lateral taper for horizontal focusing

Waveguide index set to 1.7, the index of stoichiometric silicon oxynitride. The lower index contrast allows for BPM calculations and reduces N–H bond absorption at 1510 nm.

Waveguide dimensions 0.9 μm square cross-section to limit polarization dependence and admit only one mode.

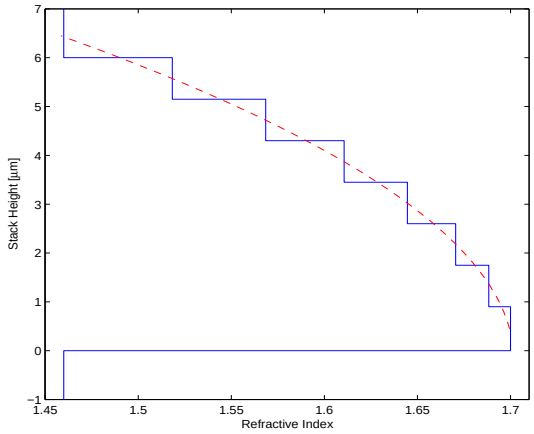

Figure 4-2: Parabolic stack index profile for the coupler.

Section 4.2 reviews some of these parameters in greater detail, including qualitatively discussing what may happen should the parameter value change.

4.1 Variable Design Parameters

The four variable parameters are the coupler dimensions needed for mask layout, specifically coupler length, input and output facet width, and lens radius of curvature. Through simulations, we found their optimal values and how deviation from these values affects coupler performance. Two or three dimensional structures were used, depending on the simulation technique (FDTD or BPM, respectively). Also, all simulations assumed infinite cladding surrounding the structures.

4.1.1 Length

The optimal coupler length is determined by the coupler's parabolic grading profile, which vertically focuses incident light into the highest index bottom layer. For our purposes, we concentrate on the first focal point of the periodic self-imaging phenomenon. Thus, the optimal length of the coupler equals the focal length of the graded index (GRIN) structure, which is halfway between the coupler input facet and the first self-image. The horizontal focal length, determined by the lens and

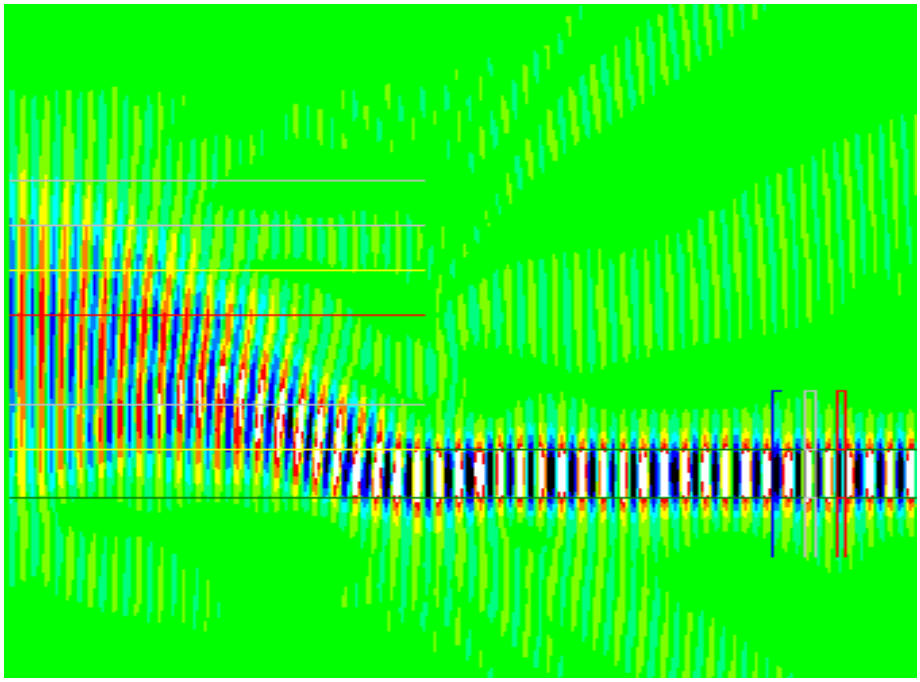

Figure 4-3: E_z distribution in a 2D GRIN structure used in FDTD coupler length simulations.

taper, is then adjusted so that it matches the vertical focal length.

We started our simulations by computing the optimal coupler length with FDTD without the influence of lenses and tapers. Simulations were run for different GRIN stack lengths for the coupler yz cross-section with the index profile seen in Figure 4-2. E_z distribution in a simulated structure is shown in Figure 4-3; most of the power enters the waveguide, but some leaks from the output facet or directly from fiber to cladding. The waveguide power is averaged across three points to remove slight fluctuations due to the presence of a second mode in the 2D slab waveguide. Because of the differing geometry in three dimensions, we expect this will not be a problem; simulations with Apollo confirm that a 3D square cross-section waveguide with similar dimensions only supports a single mode. Results are plotted in Figure 4-4 and show an optimum length of 19.5 μm. If the coupler is shorter or longer than ideal, light is no longer focused in the bottom layer where it connects to the waveguide and power leaks into the cladding.

With BPM, coupler length is calculated from peaks in mode overlap between the electric field of a 3D box coupler (*i.e.* no taper) and either the fiber or the

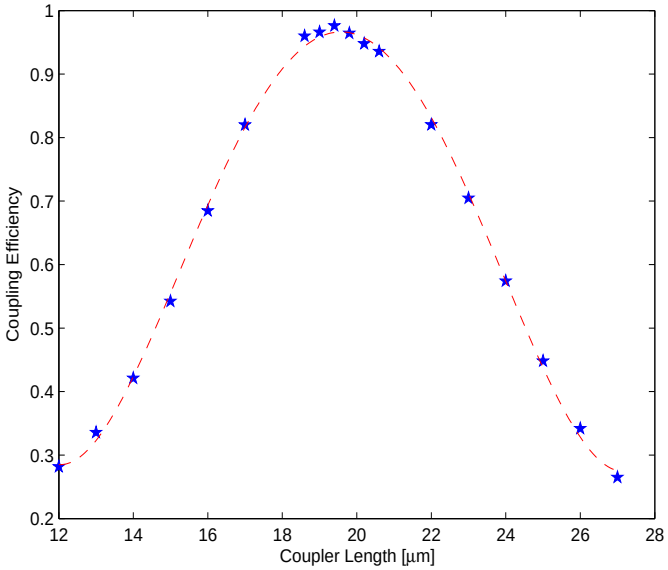

Figure 4-4: FDTD coupling efficiency versus coupler length.

waveguide fundamental mode, as defined by Equation (3.21). Only one simulation run is necessary, compared with the multiple runs—one for each data point—FDTD requires. Figure 4-5 shows how both overlaps change with propagation distance. For overlap with the waveguide mode, the peak at 20.6 μm denotes optimal length; for the fiber mode, the self-imaging peak occurs at 40.8 μm, approximately twice the coupling length. The optimal length calculated by BPM is slightly larger than that calculated by FDTD because of the approximations—most notably the paraxial approximation—made by the former method.

Ray transfer matrices provide a sanity check estimate for coupling length, defined as the convergence point of parallel rays entering a quadratic-index medium at normal incidence. When we use Equation (3.26) to calculate the vertical position of a ray as a function of propagation distance, we find that our coupler would have to be 17.4 μm long. Despite use of the same paraxial approximation as BPM, the result from ray matrix calculations is shorter than that from FDTD. We suspect this is due to the difference in grading profile. FDTD and BPM use an step parabolic, whereas ray matrices are derived based on a continuous function so rays always see an index gradient, which forces them to converge faster.

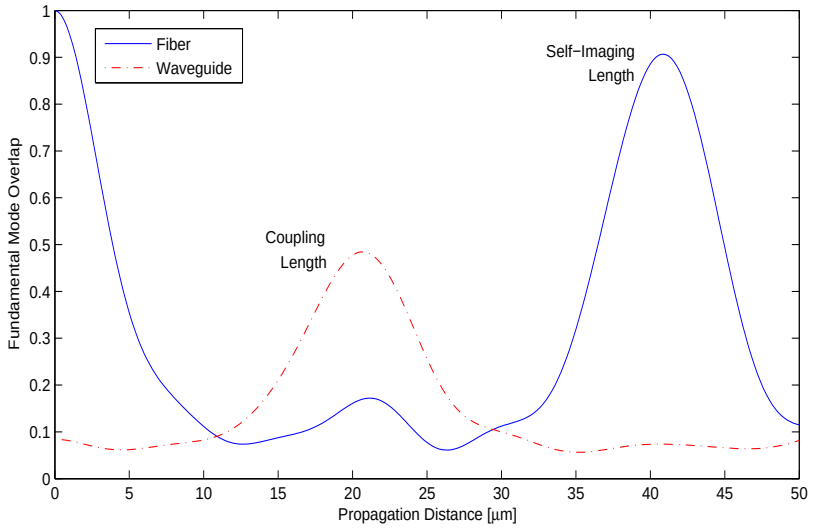

Figure 4-5: BPM overlap of box coupler field with waveguide and fiber fundamental modes.

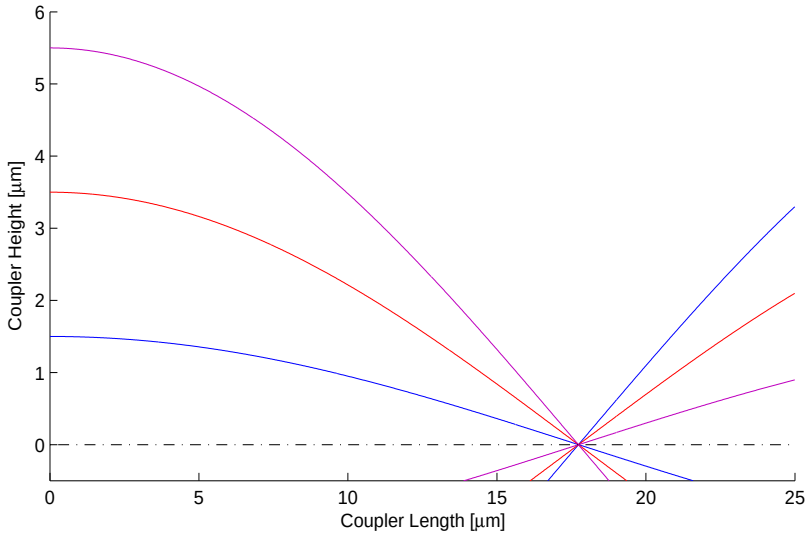

Figure 4-6: Path of rays after entering a quadratic GRIN structure (centered at $y = 0$).

Of our three approaches to calculating the vertical focal length, FDTD is probably the most accurate because it makes the fewest assumptions, and BPM the second best. This leads us to choose a length of 19.5 to 20 μm as the optimal value for our coupler and the value we will use for mask layout.

4.1.2 Facet Width

To find the optimal coupler width, we used BPM to minimize mode mismatch between the fiber and the coupler input facet, and again between the coupler output facet and the waveguide. We did not take index matching into account because our coupler design depends on a graded stack. Consequently, its performance may suffer from Fresnel reflections due to the index difference across the interface (see Equations (2.3) and (2.4)). If necessary we can later remedy this by use of an anti-reflection coating on the input facet.

For the input facet, the fiber mode is sent through a 3D box coupler and peak height at the self-imaging length plotted as a function of box width (Figure 4-7, left). We omitted the lens for this simulation because, as we later see, the optimal lens assumes the minimum possible radius of curvature allowed by the coupler width. Also, from a processing standpoint, we prefer to keep width and lens optimizations separate should the lens prove difficult to fabricate. The optimal input facet width is 7.7 μm. Loss at small widths is due to a combination of power leaking into the cladding from a wider fiber core and mode mismatch because the coupler fundamental mode is more tightly confined than that of the fiber. At larger widths, cladding loss to the left and right of the coupler decreases but mode mismatch remains, as the coupler mode is horizontally elongated. Eventually, the coupler becomes so wide that light from the fiber no longer interacts with the sidewalls and loss plateaus.

The output facet width is determined by propagating light through a 20.6 μm-long, linearly tapered coupler—both with and without a lens—and optimizing for overlap once the light has entered the waveguide. When waveguide and facet width are equal, mode mismatch decreases as width increases. In this case, the output width is restricted by the waveguide single mode condition. If instead we fix the waveguide

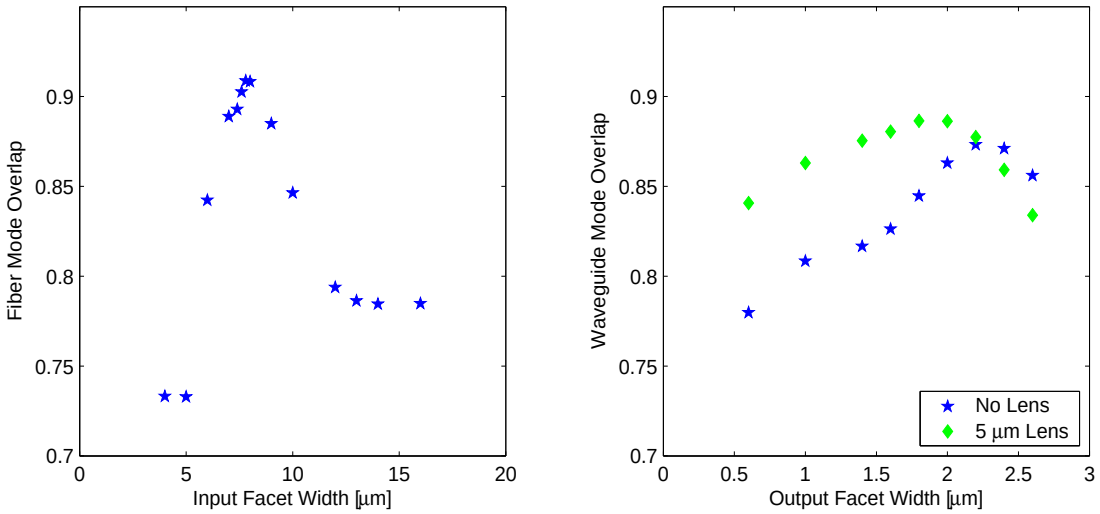

Figure 4-7: BPM coupling efficiency versus input and output facet width.

dimensions to 0.9-μm and vary the facet width, overlap with the waveguide mode peaks between 1.6 and 2.3 μm (Figure 4-7, right), depending on whether a lens is present and its radius of curvature. This result is verified through FDTD simulations. Figure 4-8 shows the electric field distribution at output facet widths of 0.9 and 2.3 μm for a taper without a lens, compared to the waveguide fundamental mode. From this, we hypothesize that the change in taper angle affects reflection off coupler sidewalls to produce an interference pattern with a single peak for the wider output facet, compared to the three peaks when taper output facet width matches that of the waveguide. This clearly indicates that the taper supports multiple modes and that a number of these are excited by the incoming light from the fiber.

In summary, optimization of mode overlap gives us 7.7 μm for the input facet width and 1.6 to 2.3 μm for the output facet width. For subsequent simulations, we set the output facet width to 0.9 μm—the waveguide width—by default because the optimal output width depends on the lens radius of curvature. The fact that the coupler supports multiple modes, a number of which are excited, implies that there will be loss from modal conversion and the inability of the waveguide to support higher order modes. Given our design and choice of fiber, modal conversion loss is inherent to the coupler, although in the future, it may be worth investigating whether different fibers excite different superpositions of modes and if some lead to lower conversion

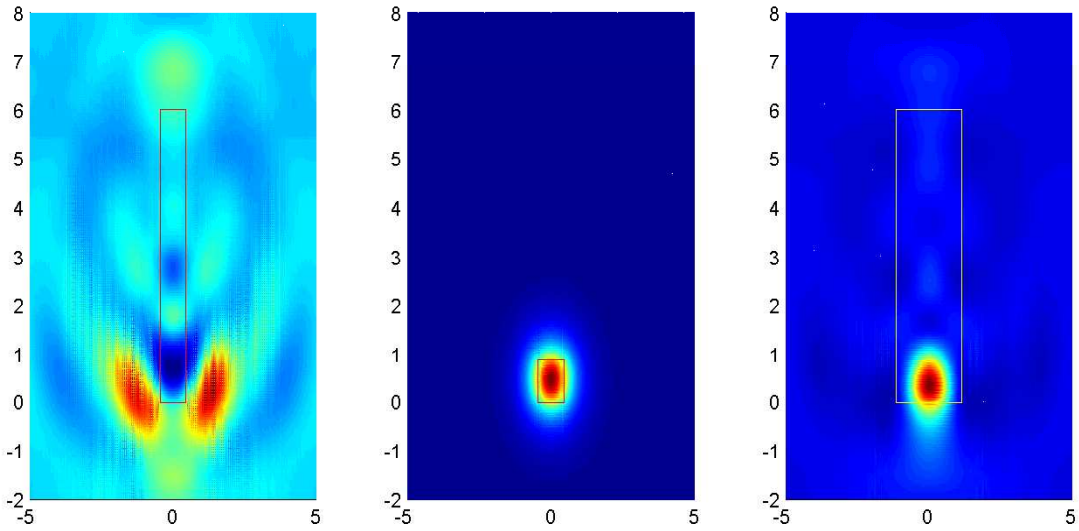

Figure 4-8: Output facet **E** distributions for a taper without a lens. Facet is 0.9-μm (left) and 2.3-μm (right) wide; waveguide fundamental mode is show in the center.

loss than others.

4.1.3 Planar Lens

The lens and taper are used to change the horizontal focal length so that it matches the vertical focal length. Between our two simulation methods, FDTD is the better method for assessing the effect of the lens on coupling efficiency because it doesn't assume paraxial propagation. Since only 2D simulations are possible, we collapsed the 3D structure to a two dimensional one by EIM; from here, the effect of lens radius of curvature on coupling efficiency was calculated. In these simulations, the total coupler length, which includes the taper and the lens, remains constant so that the vertical focal length is preserved. Also, we chose to fix the widths of the input and output facets and leave the taper angle to change based on the taper length.

2D Core Index

To calculate the 2D core index with the effective index method (EIM), we first have to find the effective index of the 3D field. This was accomplished with BeamPROP's mode solver, which propagates a field through a structure with z-invariant geometry

until the desired mode is either amplified or extracted using a correlation function. Because of the coupler's tapered geometry, the effective index varies with propagation distance so we have to repeat the mode solving process for the different widths.

Since EIM can only deal with a single mode, we chose to work with the coupler's fundamental mode because it is the dominant mode excited in the collapsed 2D structure. Using BeamPROP, we determined the effective index and entered these values into a Matlab script, written to solve the EIM transcendental equation (Equation (3.34)) and calculate n_{core}. Both index values are plotted in Figure 4-9 for the taper and waveguide. Initially, the effective index of the fundamental mode is almost constant, provided most of the mode is in the core. As width decreases, the mode is squeezed out into the cladding, which causes effective index to drop. From an index matching standpoint, this is beneficial because it brings the coupler effective index closer to that of the waveguide so reflection loss is at most 0.004 dB. To place an anti-reflection coating at this facet to attain 100% transmission would likely be too difficult and the small increase in efficiency not worth the effort.

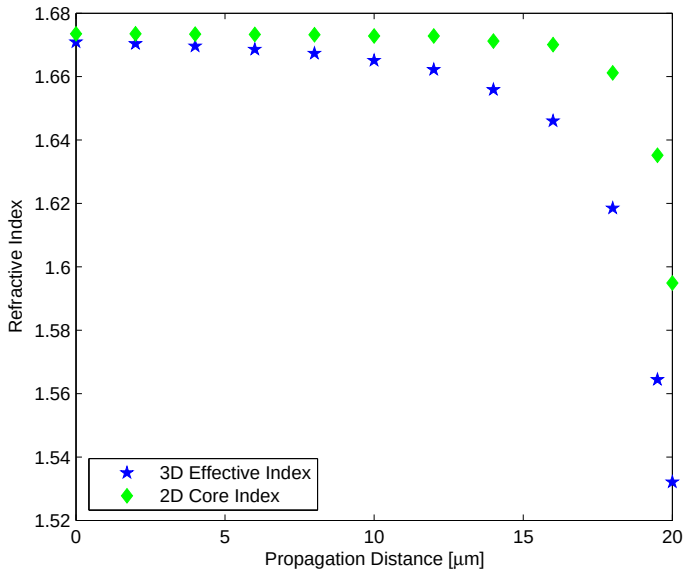

Figure 4-9: Plot of 3D effective index from BeamPROP's mode solver and 2D core index of a tapered coupler.

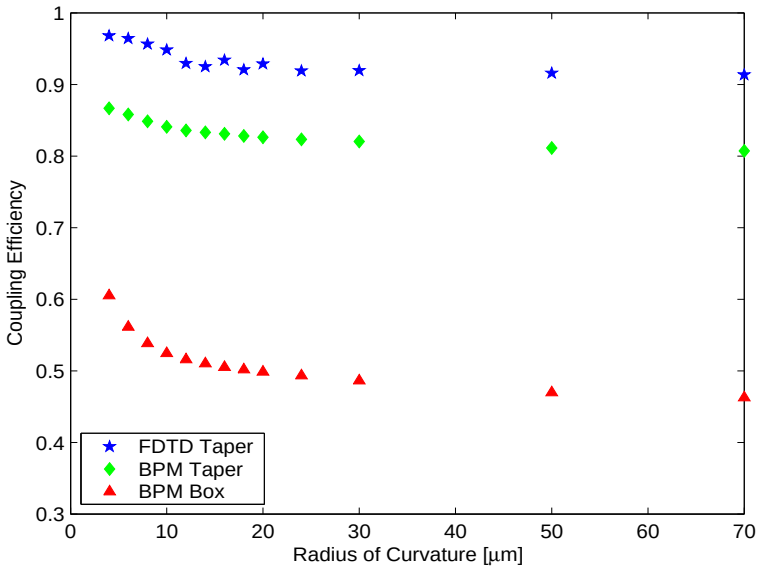

Figure 4-10: Optimization of lens radius of curvature using FDTD and BPM for box and tapered couplers.

Optimization

Once we obtained the 2D core indices, we entered them into a FullWAVE CAD file for 2D FDTD simulations to determine the optimal radius of curvature for the lens. For simplicity, the lens was assumed to have a constant core index equal to that at the taper input even though its cross-section rapidly changes with propagation distance. FDTD coupling efficiency peaks at the minimum radius of curvature—around 4 μm—before asymptotically decreasing to 0.92 as the radius approaches infinity (Figure 4-10, stars). The basic trend is verified in by 3D BPM simulations with both box and tapered couplers, as well as by ray transfer matrices. Ultimately, we chose a 5 μm radius lens so the curvature would not be as tight as a 4 μm lens, but lose in coupling efficiency would be minimal.

If the lens and the taper are considered separately, BPM simulations show that the lens alone focuses light into a waveguide more efficiently than a simple box structure, but less so than the taper without a lens. As can be seen from Figure 4-10, tapered couplers produce consistently higher overlap—and therefore coupling efficiency—with the waveguide mode for all lens radii compared to box couplers. The lens improves the performance of a tapered coupler by 0.5%, but that of a box coupler by 3.8%. Once

the taper and lens are in place, performance can be further improved by optimizing the output facet width, as was done in Section 4.1.2.

4.2 Fixed Design Parameters

In addition to dimensions, there are several other parameters that influence the propagation of light through the coupler. Due to fabrication or measurement limitations though, we have chosen to fix these parameters at appropriate values. We reviewed them at the beginning of the chapter but in this section have selected a few to discuss in greater detail.

4.2.1 Design Wavelength

In telecommunications, 1310 and 1550 nm are the wavelengths of interest because of their high transmission through silicon dioxide. We chose to optimize the coupler structure for 1550 nm light. BPM simulations indicate that vertical focal length changes minimally with wavelength (20.5 μm for 1310 nm compared to 20.6 μm for 1550 nm) and neither does coupling efficiency (Figure 4-11). Therefore, we expect that our coupler will perform reasonably well at 1310 nm even though it was not optimized for that wavelength. One benefit of wavelength insensitivity is that the same coupler can be used in triplexors for fiber to the home (FTTH) applications. These devices rely on 1310, 1540, and 1560 nm light. If an even broader range of wavelengths is desired, coupler and waveguide dimensions may require modification, but the same GRIN stack can still be used so the fabrication process change is limited to the mask layout and all devices can be fabricated on a single substrate.

4.2.2 Stack Parameters

Process design has also played a role in our decision to fix certain parameters. For instance, we chose a half-parabolic profile instead of a full profile centered on the waveguide to simplify fabrication. The half-profile has roughly the same effect on light

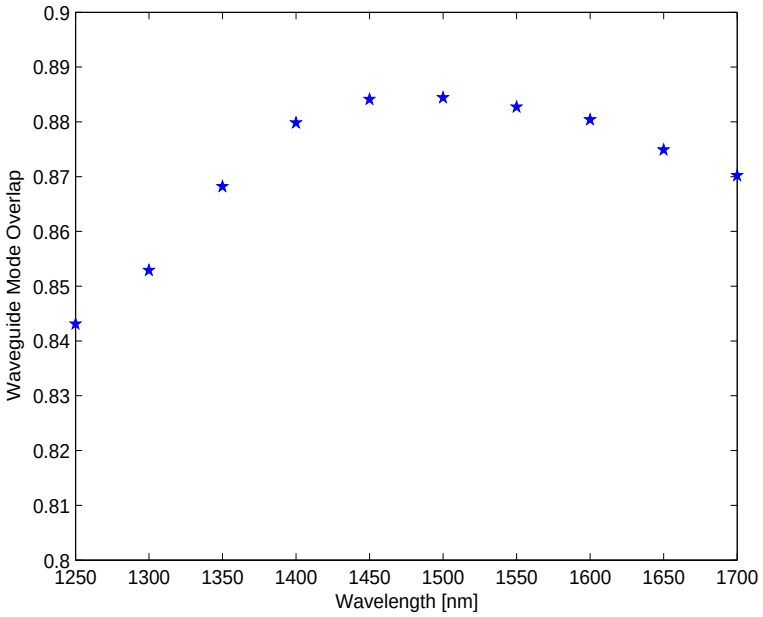

Figure 4-11: Efficiency dependence on wavelength for the optimized 1550 nm coupler.

propagation as described in Section 2.1.2, but we can avoid growing and patterning an additional graded stack under the waveguide. Since our fabrication experiments focused on etching a 6-μm stack (above the waveguide) with a poly-silicon hard mask, we chose this height for our simulations. Increasing the GRIN stack height would decrease mode mismatch and increase coupling efficiency (to some extent); however, we would also have to develop a new fabrication process to accommodate the film stress and sloped sidewalls (see Section 5.3.5) that accompany use of a thicker stack.

4.2.3 Material Selection

To grow the stack, we rely on dielectric chemical vapor deposition (DCVD) equipment, which is capable of depositing fully dense, uniform silicon oxynitride films. We selected this material for a few reasons, one being that the coupler is designed for telecommunication wavelengths and therefore should not absorb light in that range. The fact that we are working towards a silicon platform for microphotonics also limits our choices to CMOS compatible materials. Finally, varying the ratio of oxygen to nitrogen allows us to deposit material with refractive indices between 1.46 (oxide) and 2.2 (nitride); we need this for the graded stack which uses indices from 1.46 to 1.7.

The bottom layer for the waveguide has an index of 1.7, the value for stoichiometric silicon oxynitride. We chose this value because of the difficulty in accurately growing a graded stack with a low index contrast between its top and bottom layers. On the other hand, higher indices correspond to a nitrogen-rich oxynitride, which inherently contains more N–H bonds that absorb light at 1510 nm. If we were to switch to higher index waveguides, we would have to adjust the grading profile and therefore coupler length, as well as use smaller waveguide dimensions to satisfy the single mode condition. High index contrast stacks also have very short focal lengths which the planar lens and taper may not be able to match.

4.3 Summary

Using FDTD and BPM, we optimized coupler dimensions under fabrication and measurement restrictions imposed on other parameters. These dimensions, important for mask layout, included length, input and output facet width, and lens radius of curvature. Optimized values, along with those for fixed design parameters are summarized in Table 4.1. The couplers on our mask layout are designed based on these values.

We can also use our simulation results to estimate coupling efficiency of the optimized device. With BPM, this simply amounts to propagating a mode through the optimized lensed taper; coupling efficiency is around 87% (0.58 dB loss). For FDTD, we have to run two simulations—one in each plane—and multiply the results. The GRIN stack alone has an efficiency of 96%, and the planar lens and taper of 98% which, combined, gives us 94% (0.27 dB loss). This represents overall loss of a single device, which includes loss due to mode conversion, radiation, and reflection, but not to material absorption or interface scattering. We believe FDTD efficiency is higher because it does not fully account for 3D mode conversion or mismatch. In our EIM calculations to collapse the structure into two dimensions, we only considered the fundamental mode; however, BPM simulations have shown that multiple modes are excited, which leads to mode mismatch and mode conversion loss, and thus a lower BPM coupling efficiency.

Variable	
Length	19.5 μm
Input Facet Width	7.7 μm
Output Facet Width	2.3 μm
Lens	5 μm

Material	
Cladding	SiO_2
Stack Core	$SiO_{1-x}N_x$
Waveguide	SiON

Fixed	
Wavelength	1550 nm
Fiber Core	6 μm
Cladding Index	1.46
Stack Height	6 μm
Stack Index	1.46 to 1.7
Taper	linear
Waveguide Dimensions	0.9 μm
Waveguide Index	1.7

Table 4.1: Design parameters

From the effective index of the fundamental mode, we can also estimate the reflection loss from each interface with Equation (2.3). At the fiber/coupler interface, loss amounts to 0.02 dB, assuming a mode propagating from an index-matching fluid ($n = 1.47$) to the coupler with $n_{eff} = 1.67$. Coupling from air increases the reflection loss to 0.28 dB. Loss at the coupler/waveguide interface is much smaller at 0.004 dB, so total reflection loss is approximately 0.024 dB. This loss is still less than 10% of the overall [FDTD] loss, which indicates that loss from mode mismatch and mode conversion are the more important concerns. On the other hand, because of the coupler's multimode nature, completely eliminating mode conversion loss will be difficult and as we have already optimized for mode mismatch, 0.58 dB may represent the fundamental performance limit for our design. It will take more work—perhaps 3D FDTD—to confirm this hypothesis.

Chapter 5

Fabrication

Although simulations are extremely useful in understanding the basics of how light interacts with different structures, they are limited to ideal cases and "perfectly fabricated" devices. Considering every design parameter and minute consequence of varying each would be too complex and time-consuming. Secondly, a simulation relies on basic principles to produce results, but if certain a phenomenon is unaccounted for (and unexpected), it cannot be a factor in the results. Consequently, fabricating a device is the best way to understand its behavior and ascertain that all effects are accounted for in the simulation. Doing so also provides a way to assess simulation limitations once measurements are compared with theory. We can then go back and conduct more refined simulations given knowledge gained from fabrication to better understand the device. In the end, simulation and fabrication form an iterative process through which a device is developed and refined.

At our current stage, simulations serve as an adequate starting point for fabrication, especially for device dimensions for mask layout. This chapter first covers the fabrication process of the coupler and how simulations and design optimization come into play for mask layout. Afterwards, the ideal device used in simulations is contrasted with the fabricated device, and potential differences and their effect on coupling efficiency discussed.

5.1 Process Flow

We plan to fabricate the coupler in MIT's Microsystems Technology Laboratories, a cleanroom facility located on campus. The Integrated Circuits Laboratory offers a class 10 environment and access to the equipment needed for the coupler process, outlined as follows:

1. Deposit oxide under-cladding on a blank n-type silicon wafer
2. Deposit a 0.9-μm thick waveguide layer and 1 μm of poly-silicon on top to serve as a hard mask
3. Pattern poly-silicon with photolithography to define waveguides
4. Deposit remainder of graded oxynitride stack and poly-silicon hard mask
5. Pattern poly-silicon to define couplers, excluding input facet
6. Dry etch into the lower cladding so couplers and waveguides are completely defined
7. Deposit of oxide over-cladding and poly-silicon hard mask
8. Pattern poly-silicon to define input facet and lenses
9. Dry etch stack to form input facet
10. Deep etch 200 μm into the silicon substrate

As mentioned in Section 4.2.3, silicon oxynitride is used for the coupler. The Applied Materials DCVD permits us to do the deposition in a single run and adjust the gas flow to account for the changes in composition. We chose a poly-silicon hard mask for the dry etches in order to minimize mask erosion, which causes sloped sidewalls. The final deep etch step serves to remove silicon substrate between the coupler input facet and the edge of the die so that during measurement, the fiber can be brought to within a couple microns of the facet.

5.2 Mask Layout

Simulation results aided in the layout of a test mask for the above fabrication process. The mask contains 150 structures, the majority of which are variations on the optimal coupler design. We also included straight waveguides for measurement system alignment and paperclips to evaluate material and bending loss. Devices are spaced 50 μm apart and will be measured with a Newport Auto-Align station that employs a fiber-to-fiber measurement technique so that insertion loss can be obtained. Our ultimate goals are to determine if the device functions as predicted and whether varying design parameters produces the same trends in coupling efficiency as our simulations indicate. We also hope to identify sources of loss and ways to improve performance.

5.3 Deviations From Ideal

Since we know that the fabricated device structure will deviate from the ideal structure used in simulations, we varied coupler dimensions on the mask so that we will be able to identify optimal parameter values and assess trends, even if they don't match those from simulations, and form a hypothesis why the difference exists. Many aspects of the ideal coupler can change in fabrication; here, we discuss, qualitatively and quantitatively, some of those that we consider important.

5.3.1 Cladding Thickness

Although infinitely thick cladding is assumed for the simulations, we determined that a 3-μm oxide layer is adequate to prevent light from leaking into the substrate. Our calculations are based on the method described in [17]. Loss exponentially decays as thickness is increased. At 3 μm, loss is around 10^{-3} dB, which is sufficiently low for our purposes. Cladding thickness of 2 μm corresponds to 0.1 dB loss.

5.3.2 Fabrication Misalignment

Because the waveguide and the coupler are defined in separate lithographic steps, their alignment in the wafer plane depends on the accuracy of the stepper. To investigate how this will effect coupling efficiency, we used BPM to displace the two components and calculate the field overlap in the waveguide (Figure 5-1). The structure simulated did not have a lens. Offset of the waveguide along the x-axis results in power loss to the cladding and in mode mismatch. Misalignment along the propagation axis creates either a gap between the coupler and the waveguide, or could trap the poly-silicon mask between the coupler layers. We only consider the gap in our simulations, but we can assume that the presence of the poly-silicon will alter the mode shape. In this case, we started with BPM and checked our results with FDTD, because BPM is unable to account for reflected waves at the additional interfaces. If stepper alignment accuracy is no worse than ± 0.25 μm in either direction, additional loss should not exceed 0.50 dB for x-axis displacement (with the wide output face) and 0.08 dB for the gap, relative to optimal coupling efficiency.

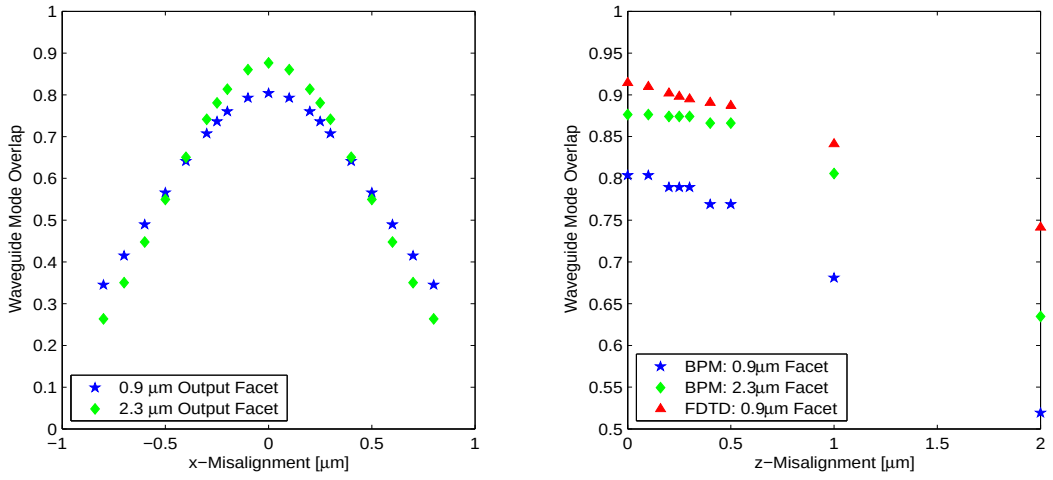

Figure 5-1: Effect of coupler-waveguide misalignment on coupling efficiency for displacement along the x and z axes.

The lens, defined in the third lithographic step, may also be offset from the coupler. An offset along the x-axis will slightly shift the focal point and some light will also enter unfocused. For a 0.25-μm displacement, this effect is minimal—no more that

0.02 dB additional loss—because if the fiber is aligned properly, light still enters the coupler rather than leaking into the cladding. Displacement along the propagation axis effectively changes the length of the coupler and should have approximately the same effect on coupling efficiency as described in Section 4.1.1, resulting in a 7×10^{-3} dB loss for a ± 0.25 μm shift.

5.3.3 Packaging Misalignment

In addition to fabrication alignment of coupler components, we also have to align the fiber to the coupler during packaging. Between fabrication and packaging misalignment, the latter is more critical because low alignment tolerance leads to high packaging costs. Coupling efficiency is optimized when both coupler and fiber centers are aligned. Horizontal and vertical displacements result in power loss to the cladding, with maximum loss determined by the packaging tool's accuracy. We used BPM to simulate the effect of displacing the fiber with respect to the coupler's input facet and plot overlap once the propagating field entered the waveguide (Figure 5-2). The plots indicate that a box structure is less sensitive than tapered couplers to fiber misalignment, but of course, coupling efficiency is lower overall. If we want to limit additional loss to ≤ 1 dB, we have to limit misalignment to no more than ± 1.36 μm in the horizontal plane, and ± 1.13 μm in the vertical plane for the tapered couplers. Because of our coupler design, neither horizontal nor vertical offset should affect focal length, assuming normal incidence of light from the fiber on the coupler facet.

To study the effect of off-normal incidence from a tilted fiber, we relied on ray transfer matrices. Because these matrices are derived under the paraxial approximation and Equation (3.26) uses a continuous function for the graded profile (rather than a step function), calculated coupling lengths do not precisely match those from simulations. However, the results can still help us understand how the structure responds to fiber angle. Focal points are approximated as the points of ray convergence.

We used Equations (3.24) and (3.26) to look at horizontal and vertical focal point shift. Focal points were calculated for incoming rays normal to the surface, $\theta = 0$, and at a slight angle, $\theta = 0.25$ to 4°. If the fiber is tilted in the vertical plane, the parabolic

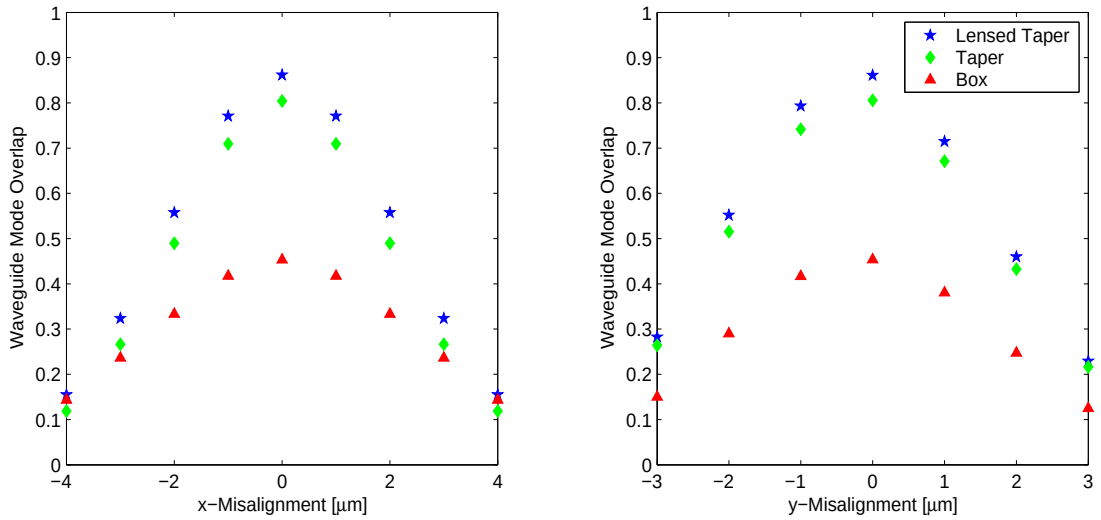

Figure 5-2: Effect of fiber-coupler misalignment on coupling efficiency for displacement along the x and y axes.

GRIN medium behaves like a lens in that its focal length remains constant but the focal point shifts vertically, as depicted by the path of rays in Figure 5-3; refraction at the cladding-coupler interface was not taken into account. For a sufficiently large angle, light will focus in the GRIN stack above the waveguide layer by the time it reaches the coupler output facet, thus reducing coupling efficiency. Fiber tilt in the horizontal plane also causes the focal point to shift without change to the focal length. However, we expect that the horizontal shift will have a smaller impact on coupling efficiency because the taper also aids in transforming the mode. The effect of horizontal (compared to vertical) fiber tilt will have to be verified with experiment because we do not have the means to easily model this situation. Figure 5-4 illustrates how the focal point of rays passing through a spherical interface changes with fiber angle.

5.3.4 Grading Profile

We consider this fabrication issue qualitatively, because we cannot predict exactly how the fabricated GRIN profile will deviate from our designed parabolic profile. As previously stated, our simulations use a parabolic profile defined in seven discrete steps, each representing a film of oxygen-rich oxynitride, with indices varying from

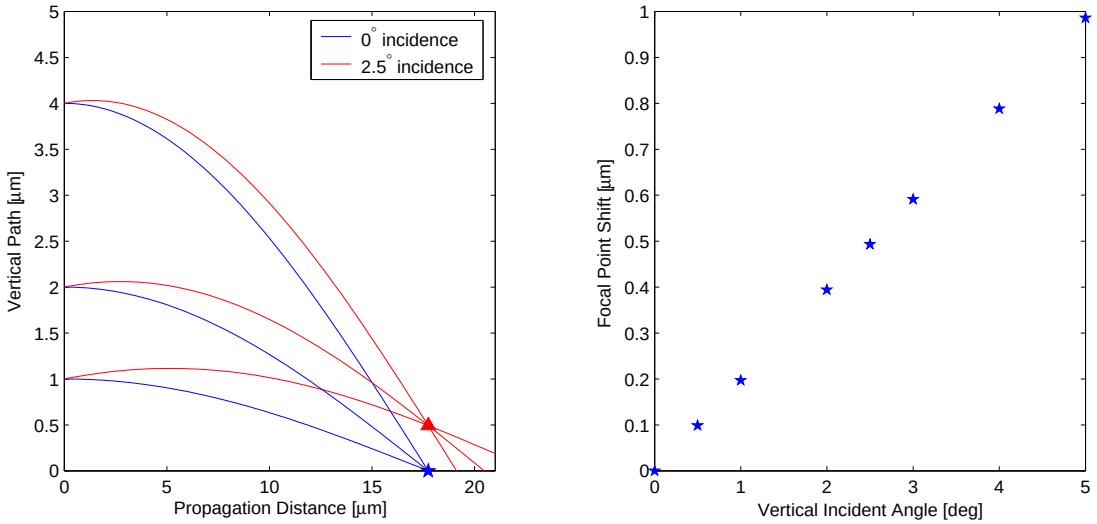

Figure 5-3: Vertical focal point shift of rays propagating through a parabolic GRIN structure centered at $y = 0$.

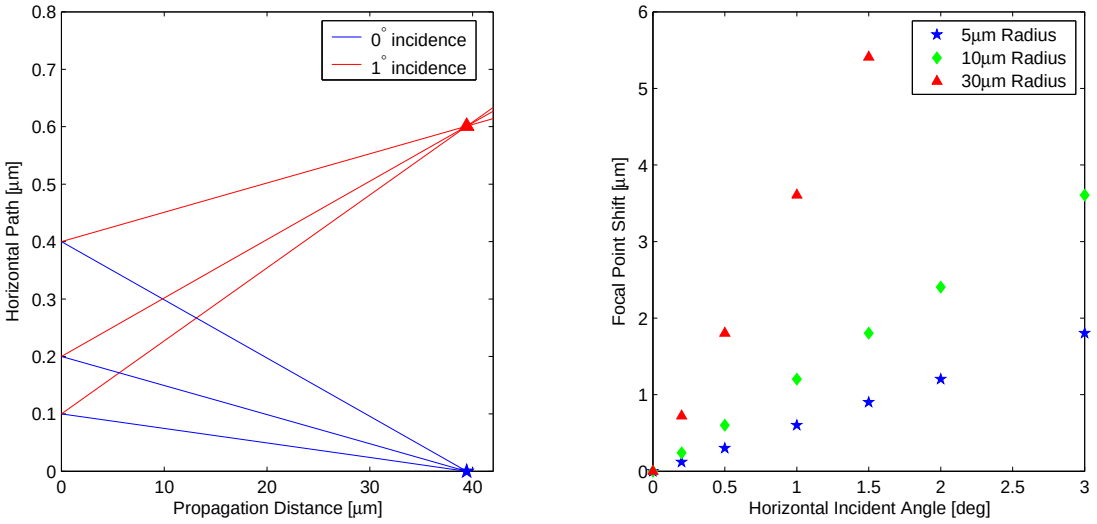

Figure 5-4: Horizontal focal point shift of rays propagating across an interface with a 5 μm radius of curvature (left) and 5, 10, and 30 μm lenses (right).

1.46 to 1.7 (*c.f.* Figure 4-2). If the index difference between the top and the bottom layers remains the same, the focal length also stays constant. Increasing this difference results in a shorter focal length because light sees a steeper index gradient and is refracted more strongly; likewise, decreasing the index difference results in a longer focal length. Deviations from a parabolic profile will result in a less defined focal point, in addition to possibly changing the focal length.

5.3.5 Sidewall Angle

Sidewall angle is also evaluated qualitatively due to the difficulty in laying out appropriate structures within the limits of the RSoft CAD program. Sloped sidewalls occur in deep etch processes when the protecting mask layer erodes around the edges. This allows variable amounts of lateral etching to occur down the sidewalls so that the top has dimensions smaller than the original mask but the base is nearly unaffected (Figure 5-5).

The presence of the slope not only changes the mode shape, but also affects light entering and exiting the coupler. Mode shape variations cause modal mismatch and can change the effective index, leading to less efficient coupling. More serious however are the slopes of the input and output facets. A slanted input facet is equivalent to tilting the fiber downward, thus causing the focal point to shift vertically. For the output facet, a sloped sidewall may result in a triangular gap between the coupler and the waveguide, even if the lithographic alignment is perfect. We could compensate for this in the mask layout by adding a predetermined overlap between the coupler and the waveguide, based on the severity of the sidewall angle. Our current mask layout does this in a few structures, but based on our simulations in Section 5.3.2, the problem may be relatively minor.

5.3.6 Material and Interface Loss

Material absorption and scattering due to core-cladding interface roughness represent other sources of loss our simulations do not account for. Although at 1550 nm loss

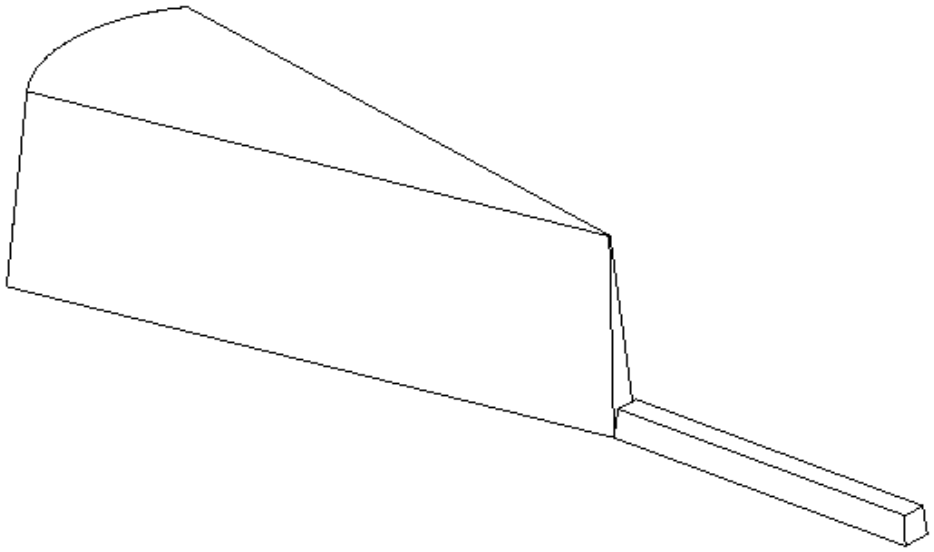

Figure 5-5: Coupler with sloped sidewalls.

reaches a minimum for silicon oxide, a small amount of absorption and [Rayleigh] scattering still occur. Also, adding nitrogen to the material not only raises its refractive index, but also increases absorption at 1510 nm due to a greater number of N–H bonds. However, given the short length of our coupler, material loss should be a minor problem: only for the waveguide might it become an issue.

Interface roughness will most likely play a larger role in reducing coupling efficiency. After the dry etch process, sidewalls may be both sloped and textured. Therefore, when light interacts with these walls, it will be randomly scattered or absorbed by electrons in interface states. If field is concentrated in the structure center and barely touches with the sidewalls (*e.g.* near the coupler input facet), scattering will not be a problem. But as the coupler tapers, the field is forced into the cladding and interaction with the interface increases.

5.4 Summary

The fabrication of a device is of particular importance if we want to determine whether or not it behaves as our simulations predict. Given the coupler structure and simulations, we have developed a fabrication process and designed a mask for use in that

Loss Source	Importance
Mode mismatch	Very important
Mode transformation	Important
Reflection loss	Unimportant
Fabrication misalignment	Important
Packaging misalignment	Very important
Changes to grading profile	Unimportant
Sidewall angle	Important
Material absorption	Unimportant
Interface scattering	Important

Table 5.1: Potential sources of loss that can decrease coupling efficiency and their relative importance to our design.

process. We then tried to evaluate how deviations from the ideal structure will affect the coupling efficiency of the fabricated device and how tolerant the structure is of these deviations. These possible sources of loss in coupling efficiency, along with mode mismatch and transformation, and reflection loss from Chapter 4, are summarized in Table 5.1. We have attempted to impart a sense of which concerns are most relevant to our design and have the potential to substantially decrease coupling efficiency if not carefully dealt with. In some cases, our sense is based on speculation and intuition because simulations would be too complex. For misalignment tolerance, we expect that fabrication misalignment loss should not exceed 0.6 dB if stepper accuracy is ± 0.25 μm. Fiber misalignment with the coupler can be no more than ± 1.13 μm overall if loss is to remain below 1 dB. As for the effect of the sidewall angle, interface roughness, and material absorption, we will have to wait for measurements of the fabricated coupler but can anticipate that the coupler is too short to cause significant loss through absorption or scattering.

Chapter 6

Design Comparisons and Discussion

There are three key requirements for a coupler: mode matching, index matching, and alignment tolerance. Other factors, however, also come into play, including the coupler's polarization dependence, the complexity of its design and fabrication process, and whether or not that process can be integrated with that of other optical components. Therefore, while a good coupler design should not only be able to perform in the first three areas, but also be feasible to fabricate.

Numerous coupler designs have been presented in literature; some of these, we review below before comparing them with our design. We also discuss our design in the context of the primary requirements of a coupler.

6.1 Fiber-to-Waveguide Couplers in Literature

The basic concept of using a coupler to transfer light between devices is not new. Several examples of fiber-to-waveguide couplers can be found in literature and present different approaches to meeting the mode transformation and index matching requirements. A number of these devices are designed for the quaternary system InGaAsP with InP cladding because of the need to couple light from laser diodes to waveguides and fibers, but the basic principles remain. We include some of the III-V compound

devices in our review to present a broader picture of coupler design.

6.1.1 Fiber End Couplers

Fiber-to-waveguide couplers can either be fabricated as part of the waveguide, such as our coupler design, or as part of the fiber. Microlenses [18] and graded index fiber tips [19] belong to the latter category. These components are either micromachined or spliced onto the end of a fiber and serve to reduce the mode spot-size. However, reducing mode size is not equivalent to mode transformation: the Gaussian mode is radially contracted rather than reshaped to the elliptical waveguide mode so loss from modal mismatch persists. Sometimes, this is considered an acceptable trade-off [20]. Also, fiber side couplers cannot account for index mismatch between their output facet and the waveguide input facet because they are typically the same material as the fiber itself. Finally, alignment tolerance becomes more critical because of the small output mode [9].

6.1.2 Waveguide End Couplers

Couplers on the waveguide end don't suffer from the same tight alignment tolerances and can potentially be designed for mode and index matching with both the fiber and the waveguide. For these reasons, the on-chip coupler is preferable. On the other hand, these devices have other drawbacks in that they are very long or difficult to fabricate.

One class of waveguide end couplers is grating couplers, which use square gratings to diffract light into a waveguide from an out-of-plane fiber in the superstrate [21, 22]. This has the benefit of being able to couple fibers to thin silicon-on-insulator (SOI) waveguides. Typically these couplers rely on long, shallow gratings, but Taillaert *et al* present a design with short, deep gratings to allow coupling perpendicular to the wafer surface [23]. The vertical fiber configuration reduces the coupler footprint, but at the same time complicates simulation and fabrication of the device. Taillaert's coupler has a theoretical efficiency of 74% but only 19% (7.2 dB) was measured;

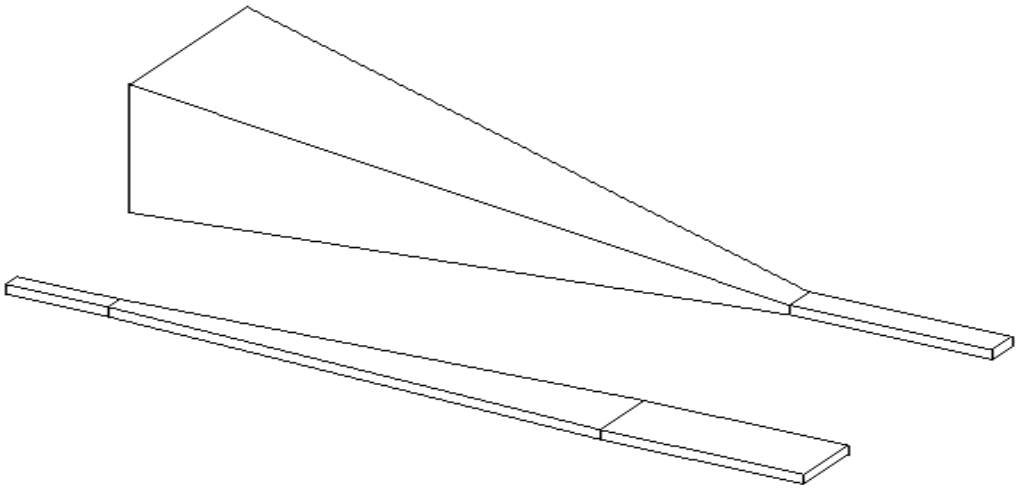

Figure 6-1: Examples of an inverse-tapered coupler (foreground) and a tapered coupler. Light from the fiber enters at the left end.

however, experimental coupling efficiency as high as 70% (1.5 dB coupling loss) has been realized [22]. Because of their small period, grating couplers described in literature were fabricated using electron-beam lithography, a time-intensive technique not suited for mass production.

Tapered couplers can potentially perform better than grating couplers, but in some cases at the expense of chip real estate or design simplicity. Most of these couplers have linear tapers, but a few rely on exponential or parabolic tapers [24, 25]. We can group these devices into two broad categories: inverse tapers, which increase from a small point at the fiber end to the waveguide dimensions, and [standard] tapers, which decrease from fiber to waveguide dimensions (Figure 6-1). More complex structures may employ combinations of the two [8].

Inverse-tapered couplers rely on a small core tip to lightly perturb the incident fiber mode; they then gradually increase to adiabatically reshape the fiber mode to that of the waveguide. The tip cross-section is optimized for mode and index matching and, for the basic inverse taper, can accommodate a misalignment up to ± 2.5 μm with no more than 1 dB additional loss [26]. Although fabrication of a lateral taper is the easiest approach, vertical tapers have been realized through processes such as shadow masking, diffusion-limited etching, and selective area growth techniques, particularly

for the InGaAsP materials system [20, 27]. Measured coupling efficiency, or loss from mode conversion, is around 0.9 dB for the basic device design [26], but can be as low as 0.4 dB [28]. The primary disadvantages of these couplers are their length, which can be anywhere from 500 to 1500 μm because of the adiabatic constraint, and their need for electron-beam lithography to define the lateral taper tip; vertical tapers also have other non-trivial fabrication requirements.

Recently, Almeida *et al* proposed and demonstrated a nanotaper which is able to couple light over 40 μm using a parabolic taper fabricated from SOI [24]. With a coupling efficiency of 0.5 dB and $\pm$1.5 μm alignment tolerance, this compact design is clearly an improvement over the long adiabatic tapers with minimal sacrifice in performance.

The remaining tapered couplers confine—rather than perturb—the incident fiber mode through total internal reflection, and force the mode to adiabatically reshape with the changing coupler dimensions. The input facet cross-section commonly has dimensions similar to those of the fiber core and the output facet, dimensions similar to those of the waveguide. Both lateral and vertical tapers are used, the latter typically fabricated with graytone lithography. Measured coupling efficiency is slightly higher than that of inverse-tapered couplers, with losses around 0.6 dB [29] or as low as 0.15 dB [30]. However, because of the SOI materials system (versus InGaAsP/InP), overall loss can significantly higher owing to interface scattering [29, 31]. Another drawback to tapered couplers is high reflection at the input facet, which arises because the coupler itself is typically fabricated from the same [high index] material as the waveguide core and the fiber from doped silica. In some cases, this can be resolved by adding an anti-reflection coating [30, 32], but such a layer may be difficult to apply. Finally, the adiabatic constraints of these couplers require that they be around 500 to 1500 μm [29, 30] in length, on par with the inverse-tapered couplers.

To reduce coupling length, Manolatou and Haus developed a tapered coupler designed to decrease beam spot-size over a few microns [9, 32]. They accomplished this with a quadratic GRIN stack for vertical, and a planar lens and lateral taper for horizontal mode-size reduction—effectively amounting to a 3D lens on the waveguide

end. Although performance is slightly compromised compared to adiabatic tapers—simulations indicate that coupling loss is around 1 dB—the advantage lies in the design's small footprint, which allows for dense optical integration. The coupler presented in this thesis is actually a variant on Manolatou's design. The differences lie in our use of lower index contrast material (oxynitride instead of silicon) for the waveguide core, and in our asymmetric GRIN stack to simplify fabrication, compared to the full, symmetric quadratic profile.

6.1.3 Comparison

As with many devices, coupler design and fabrication involve trade-offs. In some ways, such as fabrication process complexity, our coupler design has improved upon its predecessor, but potentially at the expense of coupling efficiency. Likewise, these two couplers are very short (5.5 and 20 μm) compared to the aforementioned adiabatic tapers, which can be upwards of 1 mm long. But while the compact couplers lend themselves very well to dense optical integration, they act more as lenses to shrink the mode—ours even introduces some asymmetry—rather than reshaping it to that of the waveguide. Adiabatic couplers, depending on their design, also have advantages and drawbacks. Compared to inverse tapers, standard tapers don't require a very fine tip or tight lithography specifications, but they typically need anti-reflection coatings, which can be difficult to deposit on vertical input facets. In some cases, coupler fabrication is just too complicated or expensive. Electron beam writing, for example, is a time-consuming and costly process so couplers that rely on this cannot be scaled for mass production (albeit today, steppers in industrial fabrication facilities could probably handle the small dimensions these couplers require). The ultimate goal in fabrication is a CMOS (complimentary metal-oxide-semiconductor) compatible process for the silicon microphotonics platform so use of III-V compounds is undesirable. Ultimately, numerous trade-offs have to be considered for the design and fabrication of a coupler—or any optical device—so in the end, performance may have to be sacrificed for a gain elsewhere.

6.2 Design Constraints

Regardless of the advantages and drawbacks of a coupler design, at the most basic level, it should be able to match and transform modes for the two components it connects, match index difference at each facet, and be tolerant of misalignment. We tried to account for the first of these criteria by varying input and output facet width to minimize mode mismatch with both the fiber and the waveguide. The mismatch was calculated based on BPM mode overlap with the fiber and the waveguide fundamental modes, respectively. Overall coupling loss is shown to be 0.58 dB for BPM and 0.27 dB for FDTD. Because FDTD cannot handle 3D mode transformation, we hypothesize the difference in these two values is due to mode conversion loss and therefore can estimate this to be around 0.3 dB. Because of our use of a GRIN stack, we consciously chose not to optimize for index matching at the input and output facets—the second criteria listed above. This results in a 0.024 dB reflection loss from both facets, based on our 3D effective index calculations of the coupler fundamental mode and incident light from an index-matching fluid. Misalignment between the fiber, coupler, and waveguide causes additional loss. Our simulations indicate that fabrication loss (offset of the waveguide from the coupler) should be less than 0.6 dB and that our design allows a packaging misalignment of ± 1.13 μm if loss is to be limited to 1 dB.

As for further design and fabrication considerations, our fabrication process relies on standard lithography and deposition techniques. Defining the lens may prove to be the most difficult task, but as simulations have shown, it may not be essential to the coupler as long as we use a lateral taper.

Chapter 7

Conclusions

Fiber-to-waveguide couplers are essential components in the emerging field of silicon photonics. They serve to efficiently transfer light from fibers to chips for on-chip signal routing and processing. In order to do this, they have to reduce loss through mode and index matching with each waveguide on either end. Additionally, couplers have to be tolerant of misalignment, especially for packaging.

This thesis presents a coupler design that relies on a graded index stack to transform the mode in one plane, and a planar lens and linear taper for transformation in the perpendicular plane. With BPM and FDTD simulation techniques, we optimized the coupler and investigated how varying design parameters affect its coupling efficiency. The results were then used to design a mask layout for device fabrication. Once processing and measurement are complete, we will be able to demonstrate whether our coupler functions as predicted and affirm (or invalidate) our simulation approach.

To simplify the simulations for coupler optimization, we chose to fix certain parameters based on fabrication or measurement preconditions. We first determined length with FDTD by propagating the fiber mode through a 2D structure and evaluating waveguide power relative to input power. Coupling efficiency reaches a maximum at 19.5 μm when light is focused in the lowest stack layer. For width, we relied on BPM to optimize mode matching between the fiber and the coupler, and again between the coupler and the waveguide. This led to an input facet width of 7.7 μm and

an output facet width of 2.3 μm without a lens. If a 5-μm lens is included, output width decreases to 1.6 μm. Finally, we used FDTD to find the optimal lens radius of curvature, but not before calculating the effective index of the mode to collapse the 3D structure into a 2D one with EIM. As it turns out, the optimal lens has the maximum possible curvature, which is limited by the input facet width. This was confirmed with BPM and ray matrix methods.

Simulations can impart an intuitive understanding on how varying design parameters affects device performance, and provide a starting point for fabrication (*e.g.* mask layout). However, they cannot tell us for certain whether the device will function as we expect; fabrication and measurement are the best ways to proving this. On the other hand, all fabrication processes introduce irregularities to the idealized simulation structure. We tried to account for some of these, including simulations of fiber-coupler offset and qualitative discussions on grading profile and sidewall angle. Simulations showed that photolithographic offset loss should $<$ 0.6 dB given stepper accuracy and that fiber-coupler misalignment tolerance is $\pm$1.13 μm if additional loss is not to exceed 1 dB. Additionally, we expect loss from material absorption and scattering due to by core-cladding interface roughness. Other sources of loss which we have not accounted may exist, but we will have to determine this from our measurement results.

BPM and FDTD predict total loss to be around 0.58 and 0.27 dB, respectively, including reflection loss of 0.024 dB. Our coupler design is based on Manolatou's coupler [9] and has the advantage of a simpler fabrication procedure and size for dense optical integration. However, the GRIN stack and lens make it more complicated to fabricate than some adiabatic couplers.

7.1 Future Work

There still remains a good deal of work to be done with our coupler, most notably fabrication and measurement. Doing so will definitively prove whether our design functions as we predict and how well it performs. And by merging fabrication and

simulation, we can gradually optimize the device through iteration. We can also look into adding an anti-reflection coating to reduce loss; simulation for this should be fairly straightforward since we can determine the index of the layer with $\sqrt{n_1 \cdot n_{eff}}$ and the layer in our CAD file. However, fabricating this layer on a curved facet may prove difficult. Additionally, we can consider non-linear tapers to better transform the mode and through theory and simulation, study which geometry will work best. Finally, further analysis of our coupler would be useful, possibly with 3D FDTD if supercomputer time can be attained. This calculation-intensive method would be another means to confirm (or disprove) our initial findings and possibly assess the reliability of 3D BPM in simulating our structure.

7.2 Looking Ahead

As we approach the limit to electronics technology, we increasingly look towards photonics to carry us forward along our current path. At present, optical fiber networks transverse the globe and transmit enormous quantities of information, but this is only the beginning. For our future, we envision an all optical network for information processing and transfer, from computer boards and chips to fiber optic cables, all connected by photons. Naturally, this network will be based on silicon because almost all the knowledge about the material and processing technology is already in place from the microelectronics industry. Secondly, if we challenge ourselves to design CMOS-compatible optical components, we will be able to monolithically integrate both photonics and drive electronics on the same chip. Already we are moving in this direction. The majority of devices a silicon photonic network requires have been demonstrated, with one exception: the silicon laser [1]. Now the task remains to prove that we can integrate these all individual components on a single die.

Within this all optical network, couplers will play an integral role because of the need to connect disparate components. Light has to be routed from lasers or other sources by fibers or waveguides, through filters, and into detectors; but to transfer it from one chip to another or from one board to another or from a board to a fiber, we

need couplers to match modes and indices. Our fiber-to-waveguide coupler is simply a piece of a wider vision and a step towards the future photonic network.

Bibliography

[1] L. Pavesi. Will silicon be the photonic material of the third millennium? *Journal of Physics: Condensed Matter*, 15(26):R1169, July 2003.

[2] ITRS. *International Techology Roadmap for Semiconductors Executive Summary*, 2001. `http://pubic.itrs.net`.

[3] L.C. Kimerling, L. Dal Negro, S. Saini, Y. Yi, D. Ahn, S. Akiyama, D. Cannon, J. Liu, J.G. Sandland, D. Sparacin, J. Michel, K. Wada, and M.R. Watts. Monolithic silicon microphotonics. In L. Pavesi and D.J. Lockwood, editors, *Silicon Photonics*, volume 94 of *Topics in Applied Physics*, page 89. Springer-Verlag, 2004.

[4] Gordon E. Moore. No exponential is forever: But "forever" can be delayed! In *IEEE International Solid-State Circuits Conference*, volume 1 of *Digest of Technical Papers*, page 20. IEEE, 2003.

[5] Gordon E. Moore. Cramming more components onto integrated circuits. *Electronics*, 38(8), April 1965.

[6] G. Masini, L. Colace, and G. Assanto. Si based optoelectronics for communications. *Materials Science and Engineering B*, B89:2, 2002.

[7] El-Hang Lee, Seung-Gol Lee, and Beom Hoan. VLSI microphotonics. In Louay A. Eldada, Randy A. Heyler, and John R. Rowlette, editors, *Optoelectronic Interconnects, Integrated Circuits, and Packaging*, volume 4652 of *Proceedings of SPIE*, page 1. SPIE, 2002.

[8] I. Moerman, P.P. van Daele, and P.M. Demeester. A review on fabrication technologies for the monolithic integration of tapers with III-V semiconductor devices. *IEEE Journal of Selected Topics in Quantum Electronics*, 3(6):1308–1319, December 1997.

[9] Christina Manolatou. *Passive Components for Dense Optical Integration Based on High Index-Contrast*. PhD thesis, Massachusetts Institute of Technology, 2001.

[10] P.-A. Bélanger. *Optical Fiber Theory*, volume 5 of *Series in Optics and Photonics*. World Scientific, JNew Jersey, 34.

[11] D.J. Griffiths. *Introduction to Quantum Mechanics*. Prentice Hall, Englewood Cliffs, NJ, 1995.

[12] J.A. Kong. *Electromagnetic Wave Theory*. EMW Publishing, Cambridge, MA, 2000.

[13] K.S. Yee. Numerical solution of initial boundary value problems involving maxwell's equations in isotropic media. *IEEE Transactions on Antennas and Propagation*, AP-14(3):302, 1966.

[14] J.P. Berenger. A perfectly matched layer for the absorption of electromagnetic waves. *Journal of Computational Physics*, 114:185, 1994.

[15] RSoft, Inc., Ossining, NY. *BeamPROP*, 2000.

[16] A. Yariv. *Quantum Electronics*. Wiley, New York, 1989.

[17] R.A. Soref. Compound optical crosspoint with low crosstalk. *Applied Optics*, 16(12):3223, 1977.

[18] H.M. Presby and C.A. Edwards. Near 100% efficient fibre microlenses. *Electronic Letters*, 28(6):582, March 1992.

[19] K. Shiraishi, A. Ogura, and K. Matsuura. Spotsize contraction in standard single-mode fibers by use of a GI-fiber tip with a high focusing parameter. *IEEE Photonics Technology Letters*, 10(12):1757, December 1998.

[20] G. Müller, B. Stegmüller, H. Westermeier, and G. Wenger. Tapered InP/InGaAsP waveguide structure for efficient fibre-chip coupling. *Electronic Letters*, 27(20):1836, September 1991.

[21] N. Eriksson, M. Hagberg, and A. Larsson. Highly directional grating outcouplers with tailorable radiation characteristics. *IEEE Journal of Quantum Electronics*, 32(6):1038, June 1996.

[22] T.W.Ang, G.T. Reed, A. Vonsovici, A.G.R. Evans, P.R. Routley, T. Blackburn, and M.R. Josey. Grating couplers using silicon-on-insulator. In G.C. Righini and S.I. Najafi, editors, *Integrated Optics Devices III*, volume 3620 of *Proceedings of SPIE*, page 79, San Jose, CA, March 1999. SPIE.

[23] D. Taillaert, W. Bogaerts, P. Bienstman, T.F. Krauss, I. Moerman, P. van Daele, and R. Baets. A high-efficiency out-of-plane fibre coupler for coupling to high index contrast waveguides. In *Proceedings of the 27th European Conference on Optical Communications*, volume 6 of *ECOC*, page 30. IEEE, 2001.

[24] V.R. Almeida, R.R. Panepucci, and M. Lipson. Nanotaper for compact mode conversion. *Optics Letters*, 28(15):1302–1304, August 2003.

[25] V. Vusirikala, S.S. Saini, R.E. Bartolo, S. Agarwala, R.D. Whaley, F.G. Johnson, D.R. Stone, and M. Dagenais. 1.55-μm InGaAsP-InP laser arrays with integrated-mode expanders fabricated using a single epitaxial growth. *IEEE Journal of selected topics in quantum electronics*, 3(6):1332–1343, December 1997.

[26] K. Kasaya, O. Mitomi, M. Naganuma, Y. Kondo, and Y. Noguchi. A simple laterally tapered waveguide for low-loss coupling to single-mode fibers. *IEEE Photonics Technology Letters*, 5(3):345, March 1993.

[27] T. Brenner and H. Melchior. Integrated optical modeshape adapters in InGaAsP/InP for efficient fiber-to-waveguide coupling. *IEEE Photonics Technology Letters*, 5(9):1053–1056, September 1993.

[28] N. Yoshimoto, K. Kawano, H. Takeuchi, S. Kondo, and Y. Noguchi. Spot size convertors using InP/InAlAs multiquantum well waveguides for low-loss single mode fibre coupling. *Electronic Letters*, 28(17):1610–1611, August 1992.

[29] M. Fritze, J. Knecht, C. Bozier, C. Keast, J. Fijol, S. Jacobson, P. Keating, J. LeBlanc, E. Fike, B. Kessler, M. Frish, and C. Manolatou. Fabrication of three-dimensional mode converters for silicon-based integrated optics. *Journal of Vacuum Science and Technology B*, B21(6):2897–2902, Nov/Dec 2003.

[30] J.J. Fijol, E.E. Fike, P.B. Keating, D. Gilbody, J. LeBlanc, S.A. Jacobson, W.J. Kessler, and M.B. Frish. Fabrication of silicon-on-insulator adiabatic tapers for low loss optical interconnection of photonic devices. In R.A. Heyler, D.J. Robbins, and G.E. Jabbour, editors, *Photonics Packaging and Integration III*, volume 4997 of *Proceedings of SPIE*, pages 157–170. SPIE, 2003.

[31] A. Sure, T. Dillon, J. Murakowski, C. Lin, D. Pustai, and D.W. Prather. Fabrication and characterization of three-dimensional silicon tapers. *Optics Express*, 11(26):3555–3561, December 2003.

[32] C. Manolatou and H.A. Haus. Compact mode-size converters for efficient coupling between fibers and integrated optical waveguides. In *Advanced Semiconductor Lasers and Applications*, 2001 Digest of the LEOS Summer Topical Meetings, pages 31–32, Copper Mountain, CO, 2001. IEEE, LEOS.